

# Reducing Thermoelastic Noise in Gravitational-Wave Interferometers by Flattening the Light Beams

Erika D'Ambrosio,<sup>1</sup> Richard O'Shaughnessy,<sup>2</sup> Sergey Strigin,<sup>3</sup> Kip S. Thorne,<sup>2</sup> and Sergey Vyatchanin<sup>3</sup>

<sup>1</sup>*LIGO Laboratory, California Institute of Technology, Pasadena, CA 91125*

<sup>2</sup>*Theoretical Astrophysics, California Institute of Technology, Pasadena, CA 91125*

<sup>3</sup>*Physics Faculty, Moscow State University, Moscow, Russia 119992*

(Dated: Received 13 September 2004)

In the baseline design for advanced LIGO interferometers, the most serious noise source is tiny, dynamically fluctuating bumps and valleys on the faces of the arm-cavity mirrors, caused by random flow of heat in the mirrors' sapphire substrates: so-called *thermoelastic noise*. We propose replacing the interferometers' baseline arm-cavity light beams, which have *Gaussian*-shaped intensity profiles that do not average very well over the dynamical bumps and valleys, by beams with *mesa*-shaped profiles that are flat in their central  $\sim 7$  cm of radius, and that then fall toward zero as quickly as is allowed by diffraction in LIGO's 4 km arms; see Fig. 2. The mesa beams average the bumps and valleys much more effectively than the Gaussian beams. As a result, if the mirrors' substrate radii and thicknesses are held fixed at 15.7 cm and 13 cm, and the beam radii are adjusted so diffraction losses per bounce are about 10 ppm, replacing Gaussian beams by mesa beams reduces the thermoelastic noise power by about a factor 3. If other thermal noises are kept negligible, this reduction will permit advanced LIGO to beat the Standard Quantum Limit (circumvent the Heisenberg Uncertainty Principle for 40 kg mirrors) by about a factor 1.5 over a bandwidth about equal to frequency; optical (unified quantum) noise will become the dominant noise source; and the event rate for inspiraling neutron star binaries will increase by about a factor 2.5. The desired mesa beams can be produced from input, Gaussian-profile laser light, by changing the shapes of the arm cavities' mirror faces from their baseline *spherical* shapes (with radii of curvature of order 60 km) to *Mexican-Hat* (MH; sombrero-like) shapes that have a shallow bump in the center but are otherwise much flatter in the central 10 cm than the spherical mirrors, and then flare upward strongly in the outer 6 cm, like a sombrero; Fig. 3. In this paper we describe mesa beams and MH mirrors mathematically and we report the results of extensive modeling calculations, which show that the mesa-beam interferometers are *not* substantially more sensitive than the baseline Gaussian-beam interferometers to errors in the mirror figures, positions, and orientations. This has motivated the LIGO Scientific Community (LSC) to adopt MH mirrors and mesa beams as an option for advanced LIGO, to be studied further. The details of our modeling calculations are presented in companion papers.

## I. INTRODUCTION AND SUMMARY

The Laser Interferometer Gravitational-Wave Observatory (LIGO) is designed to support successive generations of interferometric gravitational-wave detectors. LIGO's first interferometers are now in operation [1], and the (negative) results of its first gravitational-wave searches have recently been published. [2]. When they reach their design sensitivity (presumably next year), LIGO's initial interferometers, together with their international partners, will reach out into the universe to distances where it is plausible, but not probable to detect gravitational waves [3]. After a planned upgrade to *advanced LIGO interferometers* (planned to begin in 2007), wave detection will be quite probable [3]. A baseline design for the advanced LIGO interferometers has recently been adopted [4], along with several options, not currently in the baseline, that merit further study and might be incorporated at a future date. This paper describes one of these options, which has been much discussed within the LIGO Scientific Community (LSC) but has not previously been presented in the published literature: the reshaping of the arm-cavity light beams so as to reduce thermoelastic noise.

## A. The Context: Noise in Advanced LIGO Interferometers

For advanced LIGO's baseline design [4], the dominant noise sources in the most interesting frequency range (above about 20 Hz) are thermoelastic noise and optical noise (also called "unified quantum noise"). Other thermal noises (most especially coating thermal noise) might, in the end, be important; but in this paper we shall assume them negligible and shall focus on the thermoelastic noise and optical noise.

In Fig. 1 we show the thermoelastic noise [5, 6], the optical noise [7, 8, 9], their sum (labeled total noise), and the standard quantum limit (SQL) for the advanced LIGO baseline design with sapphire mirrors [4]. This figure suggests (as is well known [7]) that, if the thermoelastic noise can be reduced significantly (and if other thermal noises can be kept negligible), then the advanced LIGO interferometers will be able to beat the SQL, and the interferometers' ranges (detectable distances) for astrophysical sources will be increased significantly.

In this paper we propose a method ("flattening the interferometers' light beams") for reducing the thermoelastic noise, we evaluate the resulting increased range for

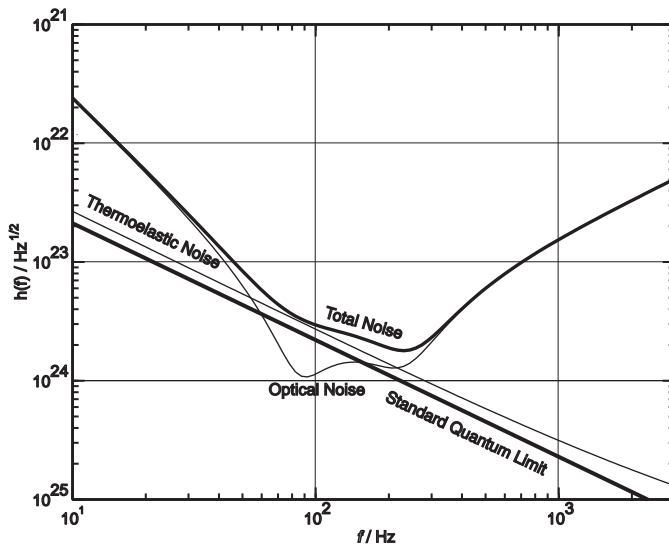


FIG. 1: Noise curves for advanced LIGO.

neutron-star / neutron-star (NS/NS) binaries, and we explore practical issues related to our proposal. We have previously discussed our proposal, the increased NS/NS range, and the practical issues in presentations at meetings of the LIGO Scientific Collaboration [10, 11, 12, 13] and in an internal LIGO document [14].

It is worth emphasizing that our proposed beam flattening need not entail any major modifications of the advanced-LIGO interferometer design; it only involves reshaping the reflecting surfaces of the test mass mirrors, adjusting the input beam, and modifying the mirror-alignment control system to account for the changes of the light-mode shapes.

### B. The Physical Nature of Thermoelastic Noise; Motivation for Reshaping Beams

Our proposal is motivated by the physical nature of thermoelastic noise. This noise is created by the stochastic flow of heat (random motions of thermal phonons) within each test mass (mirror), which produces stochastically fluctuating hot spots and cold spots inside the test mass. The test-mass material (sapphire for the baseline design of advanced LIGO) expands in the hot spots and contracts in the cold spots, creating fluctuating bumps and valleys on the test-mass (mirror) faces. These face bumps influence the light beam’s measurement of the test masses’ positions: the interferometer’s output phase shift is proportional to the difference of the test masses’ average positions — with the average being the position of a mirrored test-mass face, weighted by the light’s energy flux (its intensity distribution).

If the intensity distribution is “flat” (nearly constant) in most regions of high intensity, then the adjacent valleys and bumps (having been created by heat flow from one to the other) will average out, giving low net thermoelastic

noise. If, instead, the energy flux is sharply changing in most regions of high flux, then the adjacent valleys and bumps will not average well and the thermoelastic noise will be high. Also, the larger is the light beam, the better will be the averaging and thus the lower will be the noise.

These considerations suggest that large-radius, flat-topped beams with steep edges (e.g. the thick curve in Fig. 2 below) will lead to much smaller thermoelastic noise than small-radius, centrally peaked beams with gradually sloping sides (e.g., the thin, Gaussian curve in Fig. 2 below).

For Gaussian beams, the influence of beam radius  $r_o$  has been quantified by Braginsky, Gorodetsky and Vyatchanin [5] (who first pointed out the importance of thermoelastic noise for sapphire test masses): the thermoelastic noise power scales as  $S_h^{\text{TE}} \propto 1/r_o^3$  (aside from small corrections due to the test masses’ finite sizes [6]). This has motivated the baseline design for advanced LIGO interferometers with sapphire test masses: the beam radius  $r_o$  is chosen as large as possible, given the demand for small diffraction losses,  $\mathcal{L}_0 \lesssim 10$  ppm per bounce in the interferometer’s arm cavities.<sup>1</sup>

The baseline design uses light beams with a Gaussian distribution of energy flux, since such beams are eigenfunctions of cavities with spherical mirrors, and spherical mirrors are a standard, well-developed technology. However, the Gaussian energy flux is far from flat: most of the energy is in regions where the flux is rapidly varying with radius (thin curve in Fig. 2 below), and correspondingly the thermoelastic noise is substantially larger than it would be with “flat-topped” beams (thick curve in Fig. 2). This has motivated a (previously unpublished) proposal by O’Shaughnessy and Thorne [10] to replace the Gaussian beams with flat-topped beams, while keeping the beam radius as large as is compatible with diffraction losses  $\mathcal{L}_0 \lesssim 10$  ppm.

### C. Summary of Analysis and Results

In Sec. II we construct an example of a flat-topped light beam — a flat-topped TEM<sub>00</sub> mode of light that will resonate in an interferometer’s arm cavity, if the test-mass mirror faces are shaped appropriately. Because the intensity distribution of our flat-topped beam resembles a mesa in the southwest American desert, we call it a *mesa beam*<sup>2</sup> (a name suggested to us by Phil Willems). To produce this mesa beam as an eigenmode of a symmetric

<sup>1</sup> The 10 ppm is dictated by the following considerations: For the baseline design there is 125 W of input power to the interferometer and 830 kW of circulating power in each arm cavity. Ten ppm of diffraction loss per bounce results in a diffraction power loss in the arm cavities of  $4 \times 10 \text{ ppm} \times 830 \text{ kW} = 33$  W, which is 25 per cent of the 125 W of input light, a reasonable value.

<sup>2</sup> It is also called a *flat-topped beam* and a *mexican-hat* or *MH beam* in the internal LIGO literature [10, 11, 12, 13, 14]

arm cavity one must give the mirror faces a shape, with a central bump and an upturned brim, that resembles a Mexican hat (or sombrero) (Fig. 3), so we call the mirrors *Mexican-hat (MH) mirrors*.

We have not optimized our mesa beams' intensity distribution so as to bring the thermoelastic noise to the lowest value possible, but in Sec. II we argue that our chosen mesa beams are likely to be close to optimal.

Figure 2 below shows the intensity distribution for our proposed mesa beam (thick curve) and compares it with the intensity distribution of the baseline Gaussian beam (thin curve), which has the same diffraction losses. Figure 3 below compares the mirror shapes that support these mesa and Gaussian beams as eigenmodes of a 4 km LIGO arm. In their inner 10 centimeters of radius, the MH mirrors that support mesa beams are much flatter than the spherical mirrors that support Gaussian beams, but in their outer 6 centimeters (the upturned brim region), the MH mirrors are far more curved.

As we shall see, this greater curvature at large radii compensates considerably for the flatter shape at small radii, enabling a mesa-beam interferometer to exhibit only modestly worse parasitic-mode behavior than a Gaussian-beam interferometer, and only modestly worse sensitivity to mirror tilts, displacements, and figure errors.

Three of us (O'Shaughnessy, Strigin and Vyatchanin; OSV [15]) have computed the substantial reductions in thermoelastic noise that can be achieved in advanced LIGO by replacing the baseline spherical mirrors and their Gaussian beams with MH mirrors and their mesa beams. The method of computation and the results are described in Sec. III. Our principal conclusion is this:

1. By switching from the baseline (BL) spherical mirrors to MH mirrors with the same cylindrical test-mass diameters and thicknesses and the same 10-ppm-per-bounce diffraction losses as the BL, one can reduce the power spectral density of thermoelastic noise by a factor 0.34 and increase the volume of the universe reachable for compact-binary inspirals, and thus also LIGO's binary inspiral event rate, by a factor 2.6. Larger improvements could be achieved by using conical test masses with enlarged inner faces (frustums; Tables III and IV and Appendix I of [15]).

One might worry that the greater flatness of the MH mirrors, in the inner 10 cm where most of the light resides, will make mesa-beam interferometers much more sensitive to errors in the orientations, positions, and figures of the mirrors. We have explored this issue in great depth, with the conclusion that *mesa-beam interferometers are not substantially more sensitive to mirror errors than Gaussian-beam interferometers*. Details of our explorations are given in companion papers by D'Ambrosio [16] and by O'Shaughnessy, Strigin and Vyatchanin [15], and our methods and conclusions are presented and discussed in Sec. IV of this paper. Our quantitative con-

clusions rely on a comparison of two *fiducial* advanced-LIGO interferometer configurations, both of which have the same  $L = 4$  km arm lengths, and the same  $R = 16$  cm coated mirror radii, and beam radii that give the same 18ppm diffraction losses off the mirrors. One configuration uses *fiducial spherical mirrors* with radii of curvature  $\mathcal{R}_c = 83$  km and so has  $g = 1 - L/\mathcal{R}_c = 0.952$ , and supports *fiducial Gaussian beams* with beam radii at the mirrors  $r_o = 4.70$  cm. (This configuration differs from the current baseline design for advanced LIGO; it is nearer an altered baseline that we recommend in Sec. III A 2.) Our second configuration uses *fiducial MH mirrors* and *fiducial mesa beams* with beam radii (defined in Sec. II A)  $D = 4b = 10.41$  cm. Our comparative conclusions for these two configurations are the following (see Sec. IV for greater detail). [Note: if we had compared the baseline Gaussian-beam configuration with a mesa-beam configuration with the same diffraction losses, we would have reached approximately the same conclusions; see, e.g., the paragraph following Eq. (4.5).]

2. Among those parasitic optical modes of a perfect arm cavity that are not strongly damped by diffraction losses, the parasite closest in frequency to the desired TEM00 mode is separated from it by 0.099 of the free spectral range in the fiducial Gaussian-beam case, and by 0.0404 of the free spectral range in the fiducial mesa-beam case; see Sec. IV C. This factor  $\sim 2$  smaller mode spacing leads to a modestly greater sensitivity of the mesa-beam interferometer to mirror tilt errors.
3. The interferometer's arm cavities are about four times more sensitive to mirror tilt when fiducial MH mirrors are used than for fiducial spherical mirrors. When all four cavity mirrors are tilted through angles  $\theta$  about uncorrelated axes, the fractions of the carrier power driven into (dipolar) parasitic modes inside the arm cavities, and driven out the dark port, are about  $0.001(\theta/0.01 \mu\text{rad})^2$  and  $0.002(\theta/0.01 \mu\text{rad})^2$ , respectively for our fiducial MH mirrors; and  $0.002(\theta/0.035 \mu\text{rad})^2$  for our fiducial spherical mirrors; Sec. IV D. This factor four greater sensitivity is not a serious issue, since it turns out that the strictest constraints on mirror tilt come from the signal recycling cavity (and, if a heterodyne output were to be used, from the power recycling cavity), and not from the arm cavities; see items 7 and 8 below.
4. The interferometer's arm cavities are about equally sensitive to transverse displacements of their end test-mass mirrors (ETM's), whether the mirror shapes are fiducial MH, or are fiducial spherical. Specifically: for uncorrelated displacements of the two ETMs through distances  $s$ , the fractions of the carrier power driven into (dipolar) parasitic modes inside the arm cavities, and driven out the interferometer's dark port, are about  $100(s/1.0\text{mm})^2$

ppm and  $190(s/1.0\text{mm})^2$  ppm, respectively, for fiducial MH mirrors; and  $100(s/1.3\text{mm})^2$  ppm and  $190(s/1.3\text{mm})^2$  ppm for fiducial spherical mirrors. For details, see Sec. IV E.

5. For MH mirror figure errors with peak-to-valley height variations  $\Delta z$  in the innermost 10 cm by radius: after the control system has optimized the mirror tilts, the fractions of the carrier power driven into parasitic modes inside the arm cavities, and driven out the dark port, are about  $0.0008(\Delta z/6\text{ nm})^2$  and  $0.0015(\Delta z/6\text{ nm})^2$ , respectively; Sec. IV F. For spherical mirrors, a figure error  $\Delta z$  about twice as large drives the same power into parasitic modes — and the relevant figure error is confined to a smaller central region of the mirror (about 7.3 cm radius for baseline spherical mirrors and 8 cm for fiducial spherical mirrors, compared to 10 cm for fiducial MH mirrors). The measured mirror figure errors in the initial LIGO interferometers are of order  $\Delta z = 3$  to 6 nm peak to valley (i.e. 1 to 2 nm rms), which suggests that the MH arm cavities' required figure errors may be achievable.
6. The most serious constraints on mirror tilt and on mirror figure accuracy come not from the arm cavities but rather from the signal recycling (SR) cavity. The SR cavity, power recycling (PR) cavity, and RF sideband cavity operate approximately in the geometric optics regime and thus are nearly insensitive to whether one uses MH or spherical mirrors; Sec. IV H. As a result, *by switching from spherical to MH mirrors, one pays only a small penalty, in terms of mirror tilt constraints and figure-error constraints.*
7. More specifically, the most severe constraints on tilt and figure error arise from the driving of signal power into parasitic modes when the signal light passes through the SR cavity. To keep the resulting loss of signal strength below one per cent in the standard wideband advanced LIGO interferometers, it is necessary to constrain the magnitude  $\theta$  of the vectorial tilts of the input test-mass mirrors (ITM's) and signal recycling mirror (SRM) to  $\theta_{\text{WB}}^{\text{sph}} \lesssim 0.024\text{ }\mu\text{rad}$  (for the fiducial spherical mirrors) and  $\theta_{\text{WB}}^{\text{MH}} \lesssim 0.016\text{ }\mu\text{rad}$  (for the fiducial MH mirrors). When an advanced interferometer is narrowbanded at  $f \simeq 500\text{ Hz}$  or  $\simeq 1000\text{ Hz}$ , the constraint must be tighter:  $\theta_{\text{NB}}^{\text{sph}} \lesssim 0.011\text{ }\mu\text{rad}$ , and  $\theta_{\text{NB}}^{\text{MH}} \lesssim 0.007\text{ }\mu\text{rad}$ . These are approximately the same as the experimentally achieved [17] constraints on LIGO-I tilt arising from the RF cavity in the absence of an output mode cleaner, and the same as the baseline constraints on tilt in advanced LIGO arising from misalignment of the input laser beam [18]. If there were no output mode cleaner in advanced LIGO and heterodyne readout were used in place of the baseline homodyne readout,

then the constraint on tilts in the RF cavity (due to mode mixing for the RF sideband light used in the readout) would be about the same as that for narrowband interferometers in the SR cavity. For the baseline homodyne readout, no such RF constraint arises. The reduction in signal strength due to all the above (item 7) tilts scales as  $\theta^2$ ; and we estimate that the above (item 7) constraints are inaccurate by a factor  $\lesssim 2$  due to ignoring correlations in the overlaps of certain parasitic modes, and for the narrowbanded interferometers, due to inaccuracy of the geometric optics approximation in the SR cavity. For details of all these issues, see Sec. IV I.

8. We characterize the analogous constraints on mirror figure error by the *peak-to-valley* fluctuations in the mirror height in the central regions of the mirrors (regions enclosing 95 per cent of the light power; radius  $\simeq 10\text{ cm}$  for fiducial MH mirrors and  $\simeq 8\text{ cm}$  for fiducial spherical mirrors), with the fluctuations averaged over  $\sim 3\text{ cm}$  (an averaging produced by breakdown of geometric optics in the SR cavity). Our estimated constraints for one per cent loss of signal strength are  $\Delta z_{\text{WB}} \lesssim 2.0\text{ nm}$  for wideband advanced LIGO interferometers and  $\Delta z_{\text{NB}} \lesssim 1.0\text{ nm}$  for narrowband, independently of whether the mirrors are MH or spherical—though the region over which the constraints must be applied is different, 10 cm radius for MH and 8 cm for spherical. The loss of signal strength scales as  $\Delta z^2$ , and our estimated constraints might be inaccurate by as much as a factor  $\sim 3$  due to exploring only one representative shape for the figure errors, due to overlaps of certain parasitic modes, and for the narrowbanded interferometer due to inaccuracy of the geometric optics approximation in the SR cavity. These are approximately the same constraints as arise (in our calculations) from the RF cavity in LIGO-I, in the absence of an output mode cleaner. If there were no output mode cleaner in advanced LIGO and heterodyne readout were used, then the constraint on figure errors in the RF cavity (due to mode mixing for the RF sideband light used in the readout) would be about the same as that for wideband interferometers in the SR cavity. For details of these conclusions, see Sec. IV J.

Among all the constraints on mirror errors that arise from our modeling, the most serious are the last ones (items 7 and 8): SR-cavity-induced constraints on mirror figure errors to avoid a one per cent loss of signal strength. These constraints are nearly independent of whether the mirrors are spherical or MH. These constraints would be relaxed if the SR cavity were made less degenerate. This could be achieved by shaping the fronts of the ITMs as lenses that bring the light (Gaussian or mesa) to a focus somewhere near the SR mirror — and also near the PR mirror.

Because MH mirrors and their mesa beams produce such a great (factor 3) reduction of thermoelastic noise power, and they increase the sensitivity to mirror errors by only modest amounts, they have been adopted as options for advanced LIGO, and they may be of value for LIGO's future international-partner interferometers. In Sec. V we describe some of the future research that is needed in order to firm up our understanding of the pros and cons of MH mirrors and mesa beams.

#### D. Notation

We here summarize some of the notation used in the remainder of this paper. The numerical values are for advanced LIGO interferometers, including sapphire test-mass substrates, with the sapphire idealized as isotropic (its properties averaged over directions).<sup>3</sup>

$b$ : Diffraction lengthscale  $b = \sqrt{\lambda L/2\pi} = 2.603$  cm for light with wavelength  $\lambda = 1.064$   $\mu\text{m}$  in the  $L = 4\text{km}$  LIGO beam tubes; equal to a symmetric Gaussian beam's minimum possible radius at the end mirrors (the radius at which the power flux has dropped to  $1/e$  of its central value).

$C_V$ : Specific heat of test-mass substrate per unit mass at constant volume [ $7.9 \times 10^6 \text{erg g}^{-1} \text{K}^{-1}$ ]

$D$ : Mesa beam radius [units cm]; Eq. (2.3)

$E$ : Young's modulus of test-mass substrate [ $4 \times 10^{12} \text{dyne cm}^{-2}$ ]

**ETM**: End test mass of an arm cavity

$H$ : Thickness of test mass [units cm]

$f$ : Gravitational-wave frequency at which noise is evaluated [units Hz]

$g$ : Arm cavity's g-factor,  $g = 1 - L/\mathcal{R}_c$  where  $L$  is arm length and  $\mathcal{R}_c$  is the (identical) radius of curvature of its mirrors

$\mathcal{F}$ : Finesse of an optical cavity

$I$ : Noise integral for a test mass, Eq. (3.2)

**ITM**: Input test mass of an arm cavity

$k$ : Wave number, equal to  $2\pi/\lambda$

$k_B$ : Boltzmann's constant [ $1.38 \times 10^{-16} \text{erg K}^{-1}$ ]

$L$ : Interferometer arm length [ $4 \times 10^5 \text{cm}$ ]

$\mathcal{L}$ : Diffraction loss in a single reflection off a mirror

$M$ : Mass of test mass [ $4 \times 10^4 \text{g}$ ]

**PRM**: Power recycling mirror

$r$  Radius in transverse plane

$r_o$ : Radius, on test-mass face, at which the *intensity* of a Gaussian light beam has dropped by a factor  $1/e$  from its central value [ $r_o = 4.23 \text{cm} = 1.63b$  for baseline design]. Note: many LIGO papers, following Siegmann[19], define the beam radius to be  $\sqrt{2}$  larger, so it is the radius at which the beam's amplitude has dropped by  $1/e$ .

$P_n$ : Fraction of interferometer's light power in mode  $n$

$R_p$ : The physical radius of a test mass [15.7cm]

$R$ : The radius of the mirror coated onto a test mass [equal to  $R_p$  or  $R_p - 8\text{mm}$ ]; also, the power reflectivity of a mirror

$\mathcal{R}_c$  Radius of curvature of a spherical mirror [units cm]

$s$ : Transverse displacement of an arm cavity's ETM

$S_h(f)$ : Spectral density of noise (thermoelastic or other) for detecting a gravitational wave  $h$  with optimal direction and polarization [units  $\text{Hz}^{-1}$ ]

**SRM**: Signal recycling mirror

$T$ : Temperature of test-mass substrate [300K]

$u$ : Electric field of some light mode or superposition of modes (renormalized to unit norm,  $\int |u|^2 d\text{Area} = 1$ ); usually evaluated at the transverse plane tangent to an ITM mirror face, with the light propagating away from the ITM. Subscripts identify the mode.

$U$ : Unnormalized electric field of some light mode.

$v$ : Same as  $u$ : Unit-normed electric field of some light mode or superposition of modes.

$\Delta z$ : The peak-to-valley mirror deformation (mirror figure error) in a mirror's central region

$\alpha_l$ : Substrate's coefficient of linear thermal expansion [ $5.0 \times 10^{-6} \text{K}^{-1}$ ]

$\alpha_{1,2}$ : Amplitude of excitation of an arm cavity's parasitic mode  $u_{1,2}$  by a tilt of the cavity's ETM; Eq. (4.3)

$\beta_1$ : Amplitude of excitation of the parasitic mode  $v_1$  by mirror figure errors; Eq. (4.16)

<sup>3</sup> The influence of mechanical anisotropies and of heat-conduction anisotropies on the thermoelastic noise have not yet been investigated, but could be large enough to be important, since the relevant parameters vary with direction by amounts of order  $\pm 5\%$  for the Young's modulus  $E$ ,  $\pm 25\%$  for  $1 - 2\sigma$ ,  $\pm 5\%$  for the heat conductivity  $\kappa$ , and  $\pm 5\%$  for the thermal expansion coefficient  $\alpha_l$ .

- $\gamma_0$  Overlap of arm cavity's fundamental mode  $u_0$  with Gaussian mode  $u_d$  that drives it; Eq. (4.2)
- $\delta_\ell$  Fraction of the light power of some perturbed field  $u'_\ell$  that is in parasitic modes; Eq. (4.29)
- $\kappa$ : Thermal conductivity of test-mass substrate [ $3.3 \times 10^6$  erg s $^{-1}$  cm $^{-1}$  K $^{-1}$ ]
- $\lambda$ : Wavelength of laser light [ $1.064 \mu\text{m}$ ]; also, in Sec. IV I 3, a function appearing in the analysis of the signal recycling cavity.
- $\rho$ : Density of test-mass substrate [ $4\text{g cm}^{-3}$ ]; also, amplitude reflectivity of signal recycling mirror
- $\sigma$ : Poisson ratio of test-mass substrate [0.23]
- $\theta$ : Angle of mirror tilt
- $\theta_{\text{diff}}$ : Diffraction angle of a Gaussian beam (the Gaussian beam's opening angle if it were to continue onward through the mirror to large distance);  $\theta_{\text{diff}} = \lambda/\pi w_o = 2[(1-g)/(1+g)]^{1/4}b/L$ , where  $w_o$  is the mode's waist radius (radius at which the *amplitude* has dropped by  $1/e$  from its central value).
- $\Theta$ : expansion (fractional volume change) of substrate
- $\omega = 2\pi f$ : Angular frequency, corresponding to the frequency  $f$  at which the noise  $S_h$  is evaluated
- $\zeta_{1,2}$ : Amplitude of excitation of an arm cavity's parasitic mode by transverse displacement of the ETM; Eq. (4.11)

## II. MEXICAN-HAT MIRRORS AND THE MESA MODES THEY SUPPORT

In this paper we study a specific variant of a mesa light beam and the MH mirrors that support it. We believe this variant to be near optimal for reduction of thermoelastic noise, but we have not carried out the (rather complex) analysis required to prove optimality.

### A. Mesa Fields

The flat-topped (mesa-shaped) eigenmode of an interferometer arm cavity, which we seek to construct, must have an intensity distribution that is nearly flat across most of the light beam, and that then falls as rapidly as possible (constrained by diffraction effects) at the beam's edges. Moreover, if (as in baseline advanced LIGO) the cavity's input test mass (ITM) and end test mass (ETM) have the same physical dimensions, then to minimize the thermoelastic noise at fixed net diffraction loss, the beam should be symmetric about the arm cavity's mid plane, so its beam radii  $D$  are the same on the two mirrors. Otherwise [since  $S_h^{\text{TE}} \propto 1/D^3$  approximately, and diffraction

losses increase exponentially rapidly with increasing  $D$ ; Eq. (8)], the mirror with the reduced beam radius and smaller diffraction loss will have its thermoelastic noise power increased, while that with the enlarged beam radius and larger diffraction loss will have its noise power decreased more modestly, leading to a net noise increase.

The fastest possible falloff, for light in an optical cavity of length  $L$ , is that on the edge of the *minimal Gaussian beam* — the Gaussian beam whose radius increases by a factor  $\sqrt{2}$  in going from the beam waist (at the cavity's center plane) to the cavity's end mirrors. This minimal Gaussian, at the mirror planes, has the following (unnormalized) form

$$U_{\text{min Gauss}}(r) = \exp \left[ \frac{-r^2(1+i)}{2b^2} \right], \quad (2.1)$$

where

$$b = \sqrt{L/k} = \sqrt{\lambda L/2\pi} = 2.603 \text{ cm}, \quad (2.2)$$

with  $L = 4 \text{ km}$  the cavity length,  $k = 2\pi/\lambda$  the wave number, and  $\lambda = 1.064 \mu\text{m}$  the wavelength of the light.

A near-optimal flat-topped eigenmode, with near-minimal thermoelastic noise, will have a constant intensity in the central region, and will fall off at its edge at approximately the same rate as the edge of this minimal Gaussian. To produce such an eigenmode, we superpose minimal-Gaussian fields, with a field density that is constant out to a radius  $r = D$  and then stops abruptly. More specifically, our chosen unnormalized eigenmode has the following form:

$$U(D, r) = \int_{\mathcal{C}_D} \exp \left[ \frac{-[(x-x_o)^2 + (y-y_o)^2][1+i]}{2b^2} \right] dx_o dy_o, \quad (2.3)$$

where  $r \equiv \sqrt{x^2 + y^2}$  and the integration is over a circle  $\mathcal{C}_D$  of radius  $D$ :  $\sqrt{x_o^2 + y_o^2} < D$ .

By carrying out the  $y_o$  integral in Cartesian coordinates, with  $y = 0$  and  $x = r$ , we obtain the following expression for  $U(D, r)$ , which we have used in much of our numerical work:

$$U(D, r) = b \sqrt{\frac{-2\pi}{1+i}} \int_{-D}^{+D} dx_o \exp \left[ \frac{-(x_o - r)^2(1+i)}{2b^2} \right] \times \text{erfi} \left[ \frac{\sqrt{D^2 - x_o^2}}{b} \sqrt{\frac{-(1+i)}{2}} \right]. \quad (2.4)$$

Here  $\text{erfi}(z) = \text{erf}(iz)/i$  is the imaginary error function.

By converting to circular polar coordinates and performing the angular integral, we obtain the following simpler expression for our unnormalized eigenmode

$$U(D, r) = 2\pi \int_0^D \exp \left[ \frac{-(r^2 + r_o^2)(1+i)}{2b^2} \right] \times I_0 \left[ \frac{rr_o(1+i)}{b^2} \right] r_o dr_o. \quad (2.5)$$

Here  $I_0$  is the modified Bessel function of order zero. Modes with other weightings of the minimal-radius Gaussians can be obtained by inserting a weighting function  $f(r_o)$  into the integrands of Eqs. (2.3) and (2.5).

In the Appendix we give some approximate formulae for  $U(D, r)$  valid at large radii. These are useful for quick, clipping-approximation computations of diffraction losses.

The squared norm of  $U(D, r)$  (the area integral of its squared modulus) is given by the following approximate formula, which is accurate to within a fraction of a per cent for  $3.0 \lesssim D/b \lesssim 6.0$  (the regime of interest to us):

$$N^2(D) \equiv \int_0^\infty |U(D, r)|^2 2\pi r dr = 4.66 - 50.58D + 62.10D^2. \quad (2.6)$$

We denote by  $u$  the normalized field on the mirror faces, and to distinguish it from a Gaussian field, we sometimes will use a subscript “mesa”:

$$u_{\text{mesa}}(D, r) = u(D, r) = \frac{U(D, r)}{N(D)}. \quad (2.7)$$

### B. Gaussian fields

The advanced LIGO baseline design uses arm cavities with spherical mirrors, which have Gaussian modes whose field at the mirror plane is (cf. [19])

$$u_G(r, r_o) = \frac{1}{\sqrt{\pi r_o^2}} \exp \left[ -\frac{r^2}{2r_o^2} \left( 1 - i \frac{b^2}{r_o^2 + \sqrt{r_o^4 - b^4}} \right) \right]. \quad (2.8)$$

Here  $r_o$  is the beam radius (at which the energy flux falls to  $1/e$  of its central value). From the phase of this field one can read off the radius of curvature of the mirrors

$$\mathcal{R}_c = L \left( \frac{r_o}{b} \right)^2 \left[ \left( \frac{r_o}{b} \right)^2 + \sqrt{\left( \frac{r_o}{b} \right)^4 - 1} \right], \quad (2.9)$$

and thence the arm cavity’s g-factor

$$g = 1 - L/\mathcal{R}_c.$$

### C. Diffraction Losses

In the baseline design of an advanced LIGO interferometer [4], the test masses are cylinders whose faces are coated with dielectric mirrors out to a radius  $R$  that is 0.8 cm less than the cylinders’ physical radii

$$R = R_p - 0.8 \text{ cm}. \quad (2.10)$$

We shall explore MH mirrors that are coated in this same manner,  $R = R_p - 0.8$  cm and also MH mirrors that are coated all the way out to the test-mass edges,  $R = R_p$ . The diffraction losses in each reflection of a cavity mode

off a mirror are given, approximately, by the *clipping approximation*

$$\mathcal{L}_{\text{clip}} = \int_r^\infty |u(r)|^2 2\pi r dr. \quad (2.11)$$

Here  $u(r)$  is the normalized field [ $u_{\text{mesa}}(D, r)$  for a mesa mode and  $u_G(r_o, r)$  for a Gaussian mode with infinite mirrors,  $R = \infty$ ].

In actuality, the mirrors’ edges at  $r = R$  modify the field thereby causing the true diffraction losses to differ from this clipping formula. The true diffraction losses have been computed by OSV [15] via a numerical solution of the eigenequation for the cavity modes, and independently by D’Ambrosio [16] using an FFT code to propagate light in the cavity. The results are

$$\begin{aligned} \mathcal{L}_0 &\simeq 0.85 \mathcal{L}_{\text{clip}} \text{ for mesa modes,} \\ \mathcal{L}_0 &\simeq 2.5 \mathcal{L}_{\text{clip}} \text{ for Gaussian modes,} \end{aligned} \quad (2.12)$$

in the parameter regime of interest — though the numerical coefficients 0.85 and 2.5 can oscillate substantially as the beam radii and mirror radii are changed. When we need high-accuracy diffraction losses (e.g. in portions of Sec. IV), we compute them with care using the cavity eigenequation [15]) or FFT code [16]).

### D. Mirrors and Normalized Flux for Mesa and Gaussian Modes

The baseline design for advanced LIGO interferometers has mirror radii  $R = 14.9$  cm and Gaussian beam-spot radii  $r_o = 1.63b = 4.23$  cm, corresponding to a diffraction loss of  $\mathcal{L}_0 = 10$  ppm and a mirror radius of curvature  $\mathcal{R}_c = 53.7$  km. The normalized energy flux  $|u_G(r_o, r)|^2$  for this baseline Gaussian field is shown in Fig. 2, and the shape of the mirror (segment of a *sphere* with radius 53.7 km) is shown in Fig. 3.

A cavity made from MH mirrors with the baseline radius  $R = 14.9$  cm and the baseline diffraction losses  $\mathcal{L}_0 = 10$  ppm has a mesa beam radius  $D = 3.43b = 8.92$  cm [computed from Eqs. (2.12) and (2.11)]. The normalized energy flux  $|u_{\text{mesa}}(D, r)|^2$  for this mesa field is shown in Fig. 2. Notice how flat the top of this intensity profile is, and how much like a mesa the profile is shaped, and notice the contrast with the Gaussian profile.

The surfaces of the MH mirrors coincide with the mesa field’s surfaces of constant phase; i.e., their height  $\delta z$  as a function of radius  $r$  is given by

$$k\delta z = \text{Arg}[u_{\text{mesa}}(D, r)], \quad (2.13)$$

where  $k = 2\pi/\lambda$  is the light’s wave number. This MH mirror shape is shown in Fig. 3. Notice the shallow bump in the middle and the flaring outer edges. This bump and flare resemble a Mexican hat (sombrero) and give the MH mirror its name.

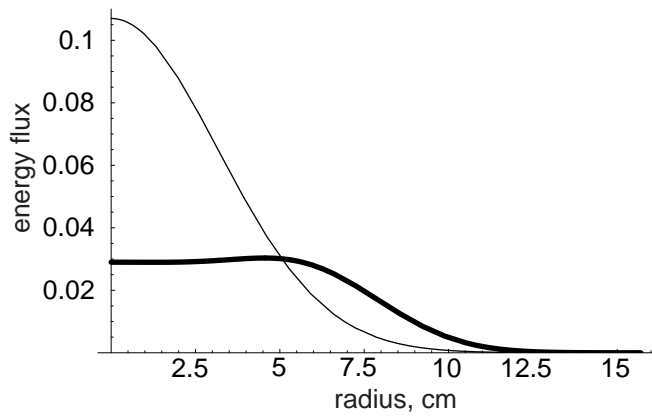


FIG. 2: The power distributions of: (i) the Gaussian mode for the baseline mirrors with coated mirror radius  $R = 15.7$  cm and beam radius  $r_o = 1.73b = 4.50$  cm (thin curve), which has diffraction loss per bounce  $\mathcal{L}_0 = 10$  ppm; and (ii) the mesa mode with  $D = 3.73b = 9.71$  cm (thick curve) which, for this same coated mirror radius  $R = 15.7$  cm, has the same diffraction loss per bounce  $\mathcal{L}_0 = 10$  ppm.

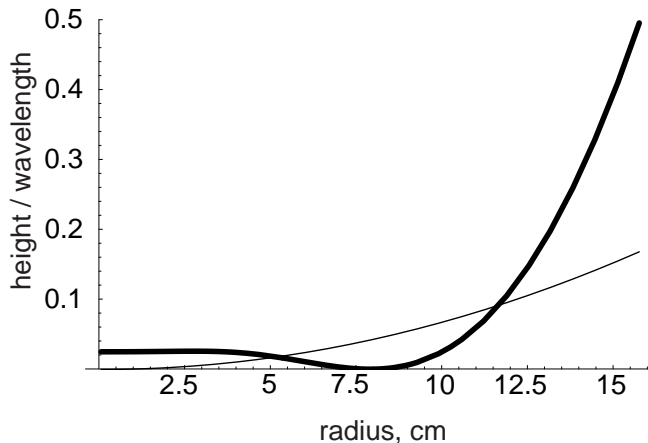


FIG. 3: The shape of the spherical mirrors (thin curve) and MH mirrors (thick curve) that support the arm-cavity Gaussian mode (thin curve) and mesa mode (thick curve) of Fig. 2. The height is measured in units of the wavelength of the light,  $\lambda = 1.064\mu\text{m}$ .

### III. THERMOELASTIC NOISE AND NEUTRON-STAR BINARY RANGE FOR MESA-BEAM INTERFEROMETERS

#### A. Thermoelastic Noise

##### 1. Quantifying the thermoelastic noise: the noise integral and the NS/NS range

Building on the seminal work of Braginsky, Gorodetsky and Vyatchanin [5], Liu and Thorne [6] have used Levin's [20] direct method to derive the following formula for an interferometers' thermoelastic noise in terms of a noise

integral  $I_A$ :

$$S_h(f) = 16\kappa k_B \left( \frac{\alpha_l ET}{C_V(1-2\sigma)\rho\omega L} \right)^2 \bar{I}; \quad (3.1)$$

where  $\bar{I}$  is the average, over the four test masses, of the thermoelastic noise integral,

$$\bar{I} = \frac{1}{4} \sum_{A=1}^4 I_A, \quad I_A = \frac{1}{F_o^2} \int_{V_A} (\vec{\nabla}\Theta)^2 d\text{volume}; \quad (3.2)$$

cf. Eqs. (3), (4) and (13) of [6]. In Eq. (3.1), the notation is as spelled out in Sec. ID, and we use numerical values (shown in Sec. ID) that assume the test-mass substrate is sapphire, idealized as an isotropic material.<sup>3</sup> In Eq. (3.2),  $\Theta$  is the expansion (fractional volume change) inside the test-mass substrate, produced by a static force with magnitude  $F_o$  and with profile identical to that of the light beam's intensity distribution over the test-mass face (e.g., Fig. 2), and the integral is over the volume  $V_A$  of test-mass  $A$ . Note that the dimensions of  $I_A$  and thence of  $\bar{I}$  are  $\text{length}/\text{force}^2 = \text{s}^4\text{g}^{-2}\text{cm}^{-1}$ .

Equation (3.1) shows that the frequency dependence of the thermoelastic noise is independent of the mirror shape and test-mass shape; it always has the same slope as the SQL (except in testbed systems with tiny mirrors and light beams [6], which are irrelevant in this paper). As a result, the thermoelastic noise produced by an advanced LIGO interferometer whose mirrors have some chosen shapes, divided by the thermoelastic noise of the baseline advanced LIGO interferometer, is equal to the ratio of the two interferometers' noise integrals

$$[S_h(f)/S_h^{\text{BL}}(f)]_{\text{TE}} = \bar{I}/\bar{I}_{\text{BL}} \quad (3.3)$$

This motivates our use of  $\bar{I}/\bar{I}_{\text{BL}}$  as one measure of a candidate interferometer's thermoelastic noise.

We shall also use a second measure: The distance to which the LIGO network can detect NS/NS binaries, with network amplitude signal-to-noise ratio 8; we call this the network's *range* for NS/NS inspirals. This three-interferometer network range is larger by a factor  $\sqrt{3} = 1.732$  than the single-4km-interferometer NS/NS range that is often used by the LIGO community and that is encoded into the "BENCH" LIGO software [21]. In computing the network range for advanced LIGO with Gaussian or mesa beams, we assume that: (i) the three advanced LIGO interferometers (all with  $L = 4$  km) are all being operated with signal-recycling-mirror parameters that maximize the range (the operation mode tentatively planned for the first year of advanced LIGO observations), (ii) they all incorporate identical sapphire mirrors with the same shapes and beam sizes, (iii) all thermal noises are negligible except thermoelastic noise, and (iv) the remaining interferometer parameters have their baseline advanced LIGO values [4] (e.g., the circulating power in each arm is 830 kW). *For the baseline advanced LIGO design with Gaussian beams, the single-4km-interferometer NS/NS range, computed under these*



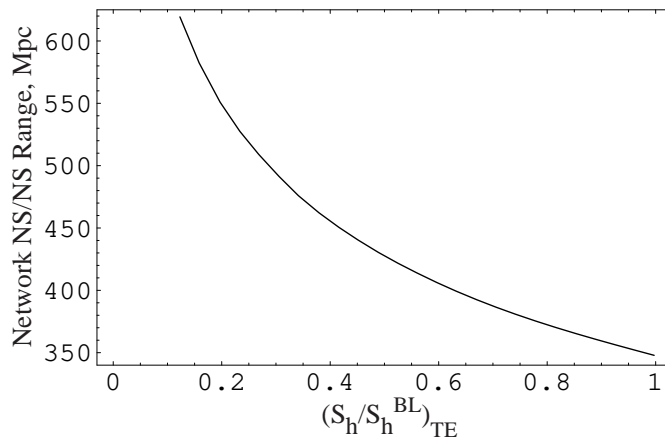


FIG. 4: The LIGO network NS/NS range as a function of the thermoelastic noise power, in units of the baseline thermoelastic noise,  $(S_h/S_h^{\text{BL}})_{\text{TE}}$ . For each thermoelastic noise level, the advanced LIGO interferometer's optical parameters (homodyne readout phase and signal-recycling mirror) are optimized to produce the greatest possible NS/NS range. The optimization has been performed for us by A. Buonanno and Y. Chen (private communication), assuming that the only significant noise sources are thermoelastic noise and optical (unified quantum) noise.

assumptions, is 200 Mpc, and the network NS/NS range is  $200\sqrt{3} = 346$  Mpc.

Since the only noise source we change, in going from one candidate interferometer design to another, is the thermoelastic noise, the NS/NS range must be some function of  $[S_h(f)/S_h^{\text{BL}}(f)]_{\text{TE}} = \bar{I}/\bar{I}_{\text{BL}}$ .

Buonanno and Chen (private communication) have performed the optimization of the advanced LIGO optical-noise parameters (the homodyne detection phase and the position and reflectivity of the signal recycling mirror), as a function of the thermoelastic-noise level, to produce for us a curve of optimized NS/NS signal-to-noise ratio  $S/N$  as a function of  $(S_h/S_h^{\text{BL}})_{\text{TE}}$ . From that  $S/N[(S_h/S_h^{\text{BL}})_{\text{TE}}]$ , we have computed the corresponding network range,  $(346 \text{ Mpc}) \times (S/N)/(S/N)_{\text{BL}}^{-1}$  as a function of thermoelastic noise. We show that range in Fig. 4.

A third measure of a candidate interferometer's performance is the ratio of its network event rate for NS/NS binaries to that of the baseline advanced LIGO network. Since the NS/NS binaries are very extragalactic, their event rate scales as the range cubed,

$$\text{Rate}/\text{Rate}_{\text{BL}} = (\text{Range}/346 \text{ Mpc})^3. \quad (3.4)$$

In a companion paper [15], OSV evaluate the thermoelastic noise integral  $I_A$  numerically for a variety of test-mass shapes and beam radii. Here we summarize the most important conclusions of those computations and their implications for our three performance parameters:  $[S_h(f)/S_h^{\text{BL}}(f)]_{\text{TE}}$  [Eq. (3.3)], NS/NS range [Fig. 4], and NS/NS event rate [Eq. (3.4)].

## 2. Baseline test masses with spherical mirrors and Gaussian beams

The baseline design of an advanced LIGO interferometer entails four identical test masses: sapphire cylinders with physical radii  $R_p = 15.7$  cm, coated-mirror radii  $R = R_p - 0.8$  cm, thickness  $H = 13$  cm, density  $\rho = 4 \text{ g cm}^{-3}$  and mass  $M = 40$  kg; and the baseline light beam at the test-mass face is Gaussian with beam radius  $r_o = 4.23 \text{ cm} = 1.63b$  so the diffraction loss per bounce is  $\mathcal{L}_0 = 10$  ppm. For this baseline beam and test mass, OSV [15] find for the value of the noise integral

$$I_{\text{BL}} = 2.57 \times 10^{-28} \text{ s}^4 \text{ g}^{-2} \text{ cm}^{-1}. \quad (3.5)$$

We advocate extending the mirror coating out to the test-mass edge so  $R = R_p = 15.7$  cm, and increasing the Gaussian beam radius correspondingly, to  $r_o = 4.49 \text{ cm} = 1.725b$ , so the diffraction losses are still 10 ppm. With this beam expansion, OSV find (Table I of [15]) that the thermoelastic noise is reduced to  $S_h/S_h^{\text{BL}} = I/I_{\text{BL}} = 0.856$  [15], from which we deduce (via Fig. 4) that the range for NS/NS binaries is increased from 346 Mpc to 364 Mpc, and the NS/NS event rate is increased by a factor  $(364/346)^3 = 1.16$ ; see Table I.

## 3. Cylindrical test masses with MH mirrors and mesa beams

OSV have computed the thermoelastic noise integral  $I$  for cylindrical test masses with mesa beams. The test masses' volumes were held fixed at the baseline value of  $10^4 \text{ cm}^3$  (masses fixed at 40 kg), while their physical radii  $R_p$  and thicknesses  $H$  were varied. For each choice of  $R_p$ , two coated-mirror radii were chosen,  $R = R_p - 8 \text{ mm}$  (the baseline choice) and  $R = R_p$  (our proposed expansion of the coating). In all cases the mesa beam radius  $D$  was that value for which the diffraction losses are 10 ppm per bounce inside the cavity.

To within the accuracy of their computations,  $\sim 0.5$  per cent, OSV (Table II of [15]) found that the thermoelastic noise integral  $I$  is minimized when the test-mass dimensions have their baseline values,  $R = 15.7$  cm,  $H = 13$  cm. In other words, the optimal test-mass shape is the same for mesa beams as for Gaussian beams. The optimized (10 ppm diffraction loss) radii  $D$  for the mesa beams, and the values of our three measures of interferometer performance are shown in Table I, in two cases: for mirrors coated out to  $R = R_p - 8 \text{ mm}$  (the baseline choice), and coated out to  $R = R_p$ .

As is shown in the table, *switching from Gaussian beams to mesa beams reduces the thermoelastic noise  $S_h \propto \bar{I}$  by about a factor 3; it increases the NS/NS range from 346 Mpc to 465 Mpc if  $R = R_p - 8 \text{ mm}$ , and 497 Mpc if  $R = R_p$ ; and it increases the NS/NS event rate by a factor  $(465/346)^3 = 2.42$  if  $R = R_p - 8 \text{ mm}$ , and to  $(497/364)^3 = 2.55$  if  $R = R_p$ .*

TABLE I: Optimized light-beam configurations, their thermoelastic noise compared to the baseline (from Table IV of [15]), their neutron-star binary range, and their event rate for NS/NS inspiral divided by the baseline rate. All test masses are assumed to be cylinders with the baseline advanced LIGO dimensions: physical radius  $R_p = 15.7$  cm and thickness  $H = 13.0$  cm. The beam radii  $r_o$  and  $D$  are chosen so that the diffraction loss per bounce in the arm cavities is 10 ppm.

Coated Radius	Beam Shape and Radius	$\left(\frac{S_h}{S_{BL}}\right)_{TE}$	NS/NS Range	$\frac{Rate}{Rate_{BL}}$
$R = R_p - 8\text{mm}$	BL: Gaussian $r_o = 4.23\text{cm}$	1.000	346 Mpc	1.00
$R = R_p - 8\text{mm}$	mesa $D/b = 3.43$	0.364	465 Mpc	2.42
$R = R_p$	Gaussian $r_o = 4.49\text{cm}$	0.856	364 Mpc	1.16
$R = R_p$	mesa $D/b = 3.73$	0.290	497 Mpc	2.97

#### 4. Conical test masses

By switching from cylindrical test masses to frustums of cones, with the same test-mass volume, one could further reduce, substantially, the thermoelastic noise and increase the NS/NS range and rate. For detailed explorations of this, see Tables III and IV and Appendix I of OSV [15].

We do not discuss this possibility in the present paper because the current technology for growing sapphire boules, from which to cut the advanced LIGO test masses, places a tight limit on the test-mass physical radius  $R_p$ . It cannot be much larger than the baseline  $R_p = 15.7$  cm; and for that maximum radius, and test-mass volumes of order the baseline  $10^4 \text{ cm}^3$ , the optimal test-mass shape is cylindrical, with the baseline dimensions [15].

When it becomes possible, in the future, to grow larger sapphire boules, it might be worth considering test masses with frustum shapes [15].

## IV. SENSITIVITY TO MIRROR TILTS, DISPLACEMENTS AND FIGURE ERRORS

The MH mirror figure (Fig. 3) is somewhat flatter than the baseline spherical mirror in its central 10 cm of radius where 95 per cent of the light power resides, but much more curved in its outer  $\sim 6$  cm. One might worry that the central flatness will cause a mesa-beam interferometer to be unacceptably sensitive to mirror-tilt-induced, mirror-displacement-induced and figure-error-induced mixing of parasitic modes into the light beam's fundamental, mesa mode. We have investigated this mode mixing and find that it is a modest problem, not a severe one. We describe our investigations and conclusions in this section. They have been described previously in our internal LIGO report [14], and a short

summary of results was given in Sec. IC above.

## A. Foundations for Investigation

### 1. Our tools of analysis

Our analysis of mode mixing and its consequences is based on three independent sets of tools. The first two sets are designed for studying the effects of mirror errors on the interferometer's high-finesse arm cavities. The third set is for analyzing the highly degenerate power-recycling and signal-recycling cavities.

*Our first tool set* (developed by Richard O'Shaughnessy with confirming calculations by Sergey Strigin and Sergey Vyatchanin, and described in detail in OSV [15]) is an *integral eigenequation* for the modes of an arm cavity. In the limit of infinite mirror radii (i.e., neglecting diffraction losses), the cavity's eigenmodes are orthonormal when integrated over the transverse plane; this is true for MH mirrors, just as for spherical mirrors (Appendix D of [15]). OSV have used their integral eigenequation to compute the modes with untilted, undisplaced and undeformed mirrors and with both infinite and finite radii. O'Shaughnessy has then tilted, displaced and deformed the ETM of one arm cavity and applied *first- and second-order perturbation theory* to its eigenequation to determine the tilt-induced and deformation-induced mode-mixing, the resulting fundamental eigenmode of the cavity with tilted and deformed ETM, its response to the driving beam, and the tilt-induced and deformation-induced power going out the interferometer's dark port. The details of these calculations are given in OSV [15]. In the following subsections we describe the main results, we compare with computations via our second tool set, and we discuss the implications for the use of MH mirrors in advanced LIGO interferometers.

*Our second tool set* (developed by D'Ambrosio and described in her companion paper [16]) is an adaptation of a standard VIRGO and LIGO *FFT code for simulating interferometers*<sup>4</sup> (a code originally designed by Patrice Hello and Jean-Yves Vinet, then further developed by Brett Bochner and others; see [22] and references therein). D'Ambrosio has used her adaptation of this code to study the same arm-cavity phenomena that OSV have studied via the cavity eigenequation and perturbation theory. She presents the details of her computations and some associated perturbation theory analyses in Ref. [16]. In the following subsections we describe her main results, we compare them with the OSV eigenequation results, and we discuss their implications.

<sup>4</sup> See <http://www.phys.ufl.edu/LIGO/LIGO/STAIC.html> where it is referred to as the FFT Full Field Relaxation Code.

Our *third tool set* (developed by Thorne and described in Secs. IV I and IV J below) is designed to deal with the influence of mirror errors on the interferometer's power-recycling and signal-recycling cavities. Because these cavities are highly degenerate, the light trapped in them and traversing them is moderately well described by the tools of geometric optics, augmented by approximate estimates of the impact of diffraction; so these are the foundation for our third tool set.

## 2. Fiducial mesa and Gaussian configurations

When analyzing practical issues, we have carried out most of our computations for *fiducial MH mirrors* that have slightly larger coated radii,  $R_M = 16$  cm, than the baseline spherical mirrors (14.9 cm at present and 15.7 cm if our recommendation to coat the outer 8 mm is followed), and we have used corresponding *fiducial mesa beams* with modestly larger diffraction losses,  $\mathcal{L}_0 = 18$  ppm, than the current baseline of about 10 ppm. In evaluating practical issues in this paper and its companions [15, 16] we will compare with *fiducial spherical mirrors* and *fiducial Gaussian beams* that have this same enlarged coated radius  $R_M = 16$  cm and diffraction losses  $\mathcal{L}_0 = 18$  ppm.

Our fiducial mirror and beam parameters, then, are as follows:

- For the *fiducial spherical mirrors*: mirror radius  $R_M = 16$  cm (vs 15.7 cm for the current baseline) and Gaussian beam radius  $r_o = 4.70$  cm (vs. 4.23 cm for the current baseline), corresponding to a mirror radius of curvature  $\mathcal{R}_c = 83$  km (vs. 53.7 km for the current baseline) and an arm-cavity g-factor  $g = 1 - L/\mathcal{R}_c = 0.952$  (vs. 0.926 for the current baseline).
- For the *MH mirrors*: mirror radius  $R_M = 16$  cm and mesa beam radius parameter  $D = 4b = 10.4$  cm, where  $b = \sqrt{\lambda L/2\pi} = 2.60$  cm, with  $\lambda = 1.064$   $\mu\text{m}$  and  $L = 4$  km the light wavelength and arm length.

[Note: if we had compared the baseline Gaussian-beam configuration with a mesa-beam configuration with the same diffraction losses, we would have reached approximately the same conclusions as we obtain from comparing these fiducial configurations; see, e.g., the paragraph following Eq. (4.5).]

## 3. Reflection and transmission coefficients

For both configurations, fiducial MH and fiducial spherical, we have assumed for the ITM mirror the advanced LIGO baseline power transmissivity  $t_I^2 = 0.995$ ; we have chosen an idealized, perfectly reflecting ETM; and for simplicity we have assumed that the only losses

are those due to diffraction, which we treat as a separate mathematical entity from the reflection and transmission coefficients. Thus, our power reflection and transmission for the ITMs and ETMs are

$$\begin{aligned} r_I^2 &= 0.995, & t_I^2 &= 0.005; \\ r_E^2 &= 1.0, & t_E^2 &= 0. \end{aligned} \quad (4.1)$$

We have also assumed the baseline advanced LIGO transmissivities and reflectivities for the power-recycling (PR) and signal-recycling (SR) mirrors; see Secs. IV I and IV J below.

## B. Driving a Mesa-Beam Interferometer with a Gaussian Beam

One way to produce the desired mesa beams in the arm cavities is to drive the interferometer with Gaussian-beam light and let the arm cavities or a mode-cleaning cavity convert the light into mesa form. One of us, ED'A (Secs. II A and II B of [16]), has identified the Gaussian beam that has the greatest overlap with the mesa beam of an MH-mirrored arm cavity. If one were to drive the MH arm cavity directly with a Gaussian beam, this would be the driving beam one would want to use. It has a beam radius  $r_{od} = 6.92$  cm, compared to our fiducial cavity's beam radius at the ITM of  $r_o = 4.70$  cm. This Gaussian driving beam  $u_d(r)$  has an overlap

$$\gamma_0^2 \equiv |\langle u_0 | u_d \rangle|^2 \equiv \left| \int u_0^* u_d d\text{Area} \right|^2 = 0.940 \quad (4.2)$$

with the cavity's fundamental mesa mode  $u_0$ , which means that 94.0 per cent of the Gaussian driving-beam light will enter the MH-mirrored cavity, and 6.0 per cent will get rejected. See Secs. II A and II B of [16], where  $\gamma_0^2$  is denoted  $\mathcal{C}^2$ .

## C. Parasitic Modes in Arm Cavities

It is useful to think of the MH mirrors as having two regions: a central region with radius  $\simeq 10$  cm, and an outer region extending from radius  $\simeq 10$  cm to radius 16 cm. In its central region, the fiducial MH mirror is much flatter than the fiducial spherical mirror; in its outer region, it is much more sharply curved; see Fig. 3. The flatness of the central region has led to concerns about degeneracies of modes and sensitivity to mirror tilts, displacements and figure errors.

O'Shaughnessy, Strigin and Vyatchanin have all independently solved the integral eigenequation for the modes of a LIGO arm cavity with fiducial MH mirrors. They have found (Sec. VII A and Table V of [15]) that *among modes that are not strongly damped by diffraction losses, the one closest in frequency to the fundamental TEM00 mode  $u_0$  is the lowest TEM01 mode (denoted  $u_1$  below).*

Its frequency separation from the fundamental is 0.0404 of the cavity's free spectral range, which is 2.5 times smaller than for the fiducial spherical-mirrored cavity,  $0.099 \times (\text{free spectral range})$ . Evidently, the sharp curvature of the MH mirrors' outer region compensates sufficiently for the flatness of their central region, to prevent the parasitic modes' frequencies from becoming near-degenerate with the fundamental.

#### D. Mirror Tilt in Arm Cavities

Our modeling predicts that *mode mixing in the arm cavities of a mesa-beam interferometer produced by tilt of the ETM's or ITM's should be of no serious consequence, if the tilt angles are kept below about  $10^{-8}$  rad.* In the following subsections we summarize the calculations that lead to this conclusion.

##### 1. Parasitic mode mixing in arm cavities

Two of us have computed the influence of a tilt of the ETM on the fundamental mode of an arm cavity: ED'A has done this using her FFT code, and RO'S has done it by applying perturbation theory to the arm cavity's integral eigenequation. The two computations agree on the following predictions:

When the ETM is tilted through an angle  $\theta$ , the cavity's fundamental mode gets changed from  $u_0(r)$  to

$$u'_0(\vec{r}) = (1 - \alpha_1^2/2)u_0(r) + \alpha_1 u_1(\vec{r}) + \alpha_2 u_2(\vec{r}) . \quad (4.3)$$

Here  $\vec{r}$  is position in the transverse plane,  $u_n$  are unit-norm superpositions of modes of the perfectly aligned cavity ( $\int |u_n|^2 d\text{Area} = 1$ ),  $\alpha_n$  are mode-mixing coefficients that scale as  $\theta^n$ , and our computations have been carried out only up through quadratic order. The maximum tilt that can be allowed is of order  $10^{-8}$  radian, so we shall express our predictions for the  $\alpha_n$  in units of  $\theta_8 \equiv \theta/10^{-8}$ .

For our fiducial spherical-mirrored cavities,  $u_0$  is the (0,0) Hermite-Gaussian mode,  $u_1$  is the (0,1) Hermite-Gaussian mode,  $u_2$  is the (0,2) mode, and the dominant mixing coefficient  $\alpha_1$  is

$$\begin{aligned} \alpha_1^{\text{sph}} &= \frac{1}{\sqrt{2}(1-g^2)^{3/4}} \left( \frac{\theta^{\text{sph}}}{b/L} \right) \\ &= \frac{\sqrt{2}}{(1+g)(1-g)^{1/2}} \left( \frac{\theta}{\theta_{\text{diff}}} \right) = 0.0064\theta_8 \end{aligned} \quad (4.4)$$

(Eqs. (62) and Appendix F of OSV [15]; cf. also Appendix A of ED'A [16]). Here  $g = 0.952$  is our fiducial arm cavity's g-factor and  $b = \sqrt{\lambda L/2\pi} = 2.603$  cm is its transverse diffraction scale.

For the MH cavity,  $u_0$  is the mesa mode shown (for slightly different beam radius) in Fig. 2; and maps of  $u_1$ , and  $u_2$ , as computed by O'Shaughnessy [15] by

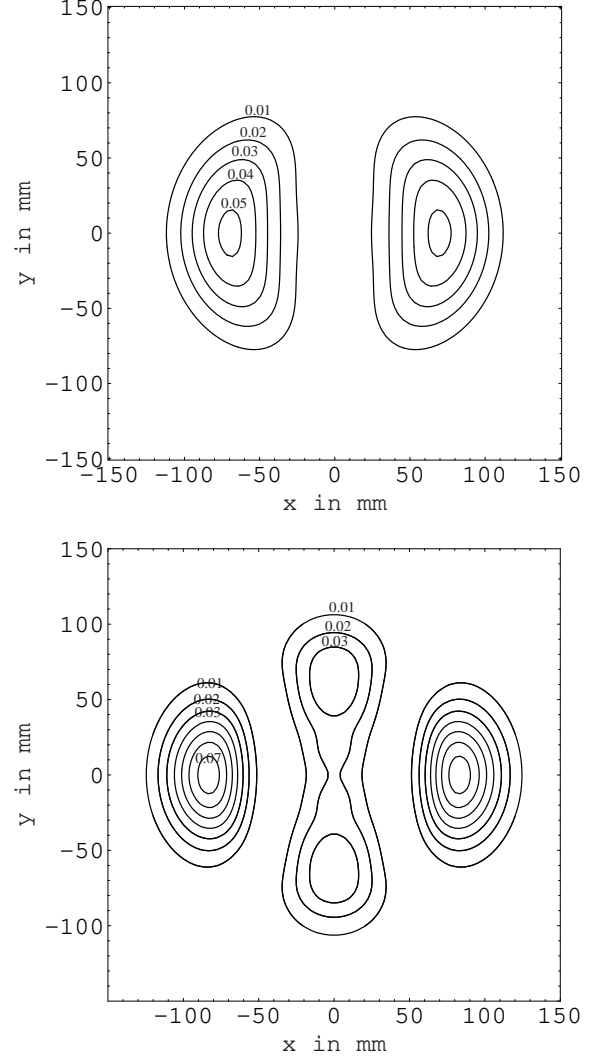


FIG. 5: Contour-diagram maps of the squared moduli  $|u_1(\vec{r})|^2$  (top) and  $|u_2(\vec{r})|^2$  (bottom) of the parasitic modes excited by tilt of the ETM of a MH arm cavity. These maps were generated by O'Shaughnessy [15] using the eigenequation for a cavity with infinite-radius MH mirrors, together with first- and second-order perturbation theory. The axis about which the ETM is tilted (rotated) is chosen to be vertical (the  $y$  axis). The units in which  $|u_j(\vec{r})|^2$  is measured are  $b^{-2} = (2.603\text{cm})^{-2}$ ; the peak values are 0.0526 for  $|u_1|^2$ , and 0.0726 for the peak of  $|u_2|^2$  on the  $x$ -axis and 0.0398 for the peak on the  $y$ -axis. The contours are separated by 0.01 in units of  $b^{-2}$ ; the outermost contour in all cases is  $0.01b^{-2}$ . See also Figs 15 and 16 of [16] for maps of these same modes as computed by ED'A with her FFT code.

solving the cavity eigenequation, are shown in Fig. 5. D'Ambrosio has used her FFT code to compute maps that agree well with these (Figs. 15 and 16 of [16]). The

MH mixing coefficients are<sup>5</sup>

$$\alpha_1^{\text{MH}} = 0.0227\theta_8, \quad \alpha_2^{\text{MH}} = 0.00019\theta_8^2 \quad (4.5)$$

(Eqs. (63) of OSV [15]; first equation on page 8 of ED'A [16]). Comparison of Eqs. (4.4) and (4.5) shows that, *to keep the dominant, dipolar mode-mixing coefficient  $\alpha_1$  at the same level in the fiducial MH cavity as in the fiducial spherical-mirrored cavity requires controlling the MH mirrors' tilt angle  $3.5 \simeq 4$  times more tightly.*

[Note: If, instead of comparing our fiducial arm cavities (Sec. IV A 2), we had compared the baseline spherical-mirrored cavity with a MH-mirrored cavity that has the same diffraction losses, we would have obtained  $\alpha_1^{\text{sph}} = 0.0047\theta_8$  (instead of  $0.0064\theta_8$ ), and<sup>6</sup>  $\alpha_1^{\text{MH}} = 0.013\theta_8$  (instead of  $0.0227\theta_8$ ). We would thereby have concluded that, to keep the dipolar mode-mixing at the same level in the MH cavity as in the spherical-mirrored cavity requires controlling the MH mirrors' tilt angle  $0.013/0.0047 = 2.8 \simeq 3$  times more tightly than the spherical mirror's tilt (rather than  $0.0227/0.0064 = 3.5 \simeq 4$  times more tightly). This illustrates the fact that the comparison of our fiducial configurations gives approximately the same answers as would a comparison that focuses on the baseline advanced-LIGO configuration.]

For our fiducial configurations, the fractional power in the dominant, dipolar parasitic mode is  $\alpha_1^2$ , which will be doubled to

$$\begin{aligned} P_1^{\text{sph arm total}} &\simeq 2(\alpha_1^{\text{sph}})^2 \simeq 0.001(\theta_8/3.5)^2, \\ P_1^{\text{MH arm total}} &\simeq 2(\alpha_1^{\text{MH}})^2 \simeq 0.001\theta_8^2, \end{aligned} \quad (4.6)$$

when the ITM and ETM are both tilted but about uncorrelated axes. This *suggests that, so far as the arm cavities are concerned (i.e., ignoring issues of tilt in the recycling cavities), the tilt of MH mirrors need not be controlled much better than  $\simeq 10^{-8}$  rad.* We have verified this by examining the effects of the mode mixing on various cavity and interferometer parameters; see the next three subsections.

## 2. Diffraction Losses

One of us (ED'A), from her FFT simulations, has estimated the influence of ETM tilt on diffraction losses to be (last equation on page 9 of [16])

$$\mathcal{L}'_0{}^{\text{MH}} = \mathcal{L}_0^{\text{MH}}(1 + 0.004\theta_8^2), \quad (4.7)$$

where  $\mathcal{L}_0^{\text{MH}} = 18$  ppm for our fiducial mirrors. This result has been confirmed to a factor  $\sim 2$  by RO'S by combining

the clipping approximation with perturbation theory of the cavity's eigenequation; Eq. (65) of [15]. The influence of ITM tilt should be about the same, thus doubling the coefficient of  $\theta_8^2$ . *This tilt-induced increase in losses is so small that it can be ignored for tilt angles below  $\sim 10^{-8}$  rad.*

## 3. Arm Cavity Gain

We have computed (ED'A via the FFT code and RO'S via perturbation theory) the following influence of ETM tilt on the arm cavity gain<sup>7</sup>

$$G_{\text{cav}}^{\text{MH}} = 740(1 - 0.00057\theta_8^2) \quad (4.8)$$

(Eq. (68) of [15]; Sec. III B of [16]). This result assumes the baseline values for the power transmissivities of the ITM and ETM, and assumes for simplicity that the only losses are diffraction losses; Sec. IV A 3. The factor 740 assumes the cavity is driven by its best-fit Gaussian beam and thus is smaller by about  $\gamma_0^2 = 0.940$  than the gain in the untilted, fiducial spherical-mirrored cavity. The tilt of the ITM should produce about the same gain reduction as that of the ETM, thus doubling the coefficient of  $\theta_8^2$  to  $\sim 0.001$ . This coefficient is small enough that *the tilt-induced decrease of MH arm-cavity gain will be negligible if  $\theta$  is controlled to  $\sim 10^{-8}$  rad.*

## 4. Dark Port Power

We have computed the influence of the tilt of one ETM on the dark-port output light (ED'A using the FFT code and RO'S using perturbation theory). Multiplying that result by four to deal with the case of all four cavity mirrors being tilted about uncorrelated axes, we find for the fraction of the interferometer's input power that winds up at the dark port in the fundamental mode  $u_0$  and the parasitic modes  $u_1$  and  $u_2$ :

$$\begin{aligned} P_0^{\text{MH DP total}} &\simeq 1.0\theta_8^4 \text{ ppm}, \\ P_1^{\text{MH DP total}} &= 4\gamma_0^2(\alpha_1^{\text{MH}})^2 \simeq 2000\theta_8^2 \text{ ppm}, \\ P_2^{\text{MH DP total}} &= 4\gamma_0^2(\alpha_2^{\text{MH}})^2 \simeq 0.1\theta_8^4 \text{ ppm}. \end{aligned} \quad (4.9)$$

(Eqs. (70) of [15] multiplied by 4; last four equations on page 8 of [16]<sup>8</sup> multiplied by 2). *Without an output mode cleaner, the dark-port power would primarily be in the dipolar mode  $u_1$ , and for  $\theta < 10^{-8}$  rad it would constitute  $< 0.2$  per cent of the input light. The planned output mode cleaner will wipe out this  $u_1$  power and the power in*

<sup>5</sup> RO'S and ED'A both find  $\alpha_1^{\text{MH}} = 0.0227\theta_8$ ; for  $\alpha_2^{\text{MH}}$  RO'S finds  $0.00018\theta_8^2$  and ED'A finds  $0.00020\theta_8^2$ .

<sup>6</sup> We thank Pavlin Savov for computing this number for us.

<sup>7</sup> RO'S finds  $G_{\text{cav}}^{\text{MH}} = 737(1 - 0.00055\theta_8^2)$ ; ED'A finds  $G_{\text{cav}}^{\text{MH}} = 746(1 - 0.00059\theta_8^2)$ .

<sup>8</sup> In [16]  $P_{\text{DP}}/P_0$  is half our  $P_1^{\text{MH DP total}}$ , and  $P_{\text{DP}}^{\text{nondip}}$  is half our  $(P_0^{\text{MH DP total}} + P_2^{\text{MH DP total}})$ .

mode  $u_2$ , leaving only the tiny fundamental-mode power, which should be totally negligible for  $\theta$  below  $10^{-8}$  rad.

For comparison, the dark-port powers with the fiducial Gaussian beams are

$$\begin{aligned} P_0^{\text{sph DP total}} &= 4(\alpha_1^{\text{sph}})^4 \simeq 1.0(\theta_8/3.5)^4 \text{ ppm} , \\ P_1^{\text{sph DP total}} &= 4(\alpha_1^{\text{sph}})^2 \simeq 2000(\theta_8/3.5)^2 \text{ ppm} , \end{aligned} \quad (4.10)$$

which shows once again that the fiducial spherical-mirrored arm cavities are  $\sim 4$  times less sensitive to tilt than the fiducial MH arm cavities.

### E. Transverse Displacement of Arm Cavities' Mirrors

When the ETM is displaced transversely through a distance  $s$ , the cavity's fundamental mode gets changed from  $u_0(r)$  to

$$u_0'(\vec{r}) = (1 - \zeta_1^2/2)u_0(r) + \zeta_1 w_1(\vec{r}) + \zeta_2 w_2(\vec{r}) , \quad (4.11)$$

where the parasitic modes  $w_n$ , like the  $u_n$ 's, have unit norm,  $\langle w_n | w_n \rangle = \int |w_n|^2 d\text{Area} = 1$ , and have phase adjusted so the coupling coefficients  $\zeta_n$  are real, and where  $\zeta_n \propto s^n$ .

R'OS has computed the coupling coefficients  $\zeta_n$  for fiducial spherical mirrors and fiducial MH mirrors by applying perturbation theory to the cavity's eigenequation; and for MH mirrors, ED'A (unpublished) has computed the influence of the ETM displacement on the arm cavity's gain using her FFT code, and has then deduced  $\zeta_1^{\text{MH}}$  by fitting to an analog of Eq. (68) of [15] in the limit of small displacements. For both spherical and MH mirrors,  $\zeta_2$  is negligible compared to  $\zeta_1$  when the displacement is  $s \ll b \equiv \sqrt{\lambda L/2\pi} = 2.60$  cm, so we shall ignore  $\zeta_2$ . From the R'OS and ED'A computations, we deduce that the fiducial MH-mirrored cavities and fiducial spherical-mirrored cavities are approximately equally sensitive to transverse displacements of the ETM; their coupling coefficients are:<sup>9</sup>

$$\begin{aligned} \zeta_1^{\text{sph}} &= \left( \frac{(1-g)^{1/4}}{\sqrt{2}(1+g)^{3/4}} \right) \frac{s}{b} = 0.008 s_{\text{mm}} , \\ \zeta_1^{\text{MH}} &= 0.010 s_{\text{mm}} . \end{aligned} \quad (4.12)$$

Here  $g = 0.952$  is the fiducial arm cavity's  $g$ -factor, and  $s_{\text{mm}}$  is the ETM's transverse displacement in millimeters. The MH cavity's lesser sensitivity to displacement

presumably arises from the flatness of its mirrors in the central region, where most of the light power resides.

The corresponding fraction of the arm-cavity carrier power driven into the (dipolar) parasitic field  $w_1$  is (cf. Eq. (59) of [15])

$$P_1^{\text{arm total}} = \zeta_1^2 \simeq \begin{cases} 100(s/1.3\text{mm})^2 \text{ ppm} & \text{spherical,} \\ 100(s/1.0\text{mm})^2 \text{ ppm} & \text{MH.} \end{cases} \quad (4.13)$$

The fraction of the input carrier power driven out the dark port when the ETMs of both arm cavities are displaced through a distance  $s$  but in uncorrelated directions is about twice the above [cf. [15], Eq. (60) multiplied by two, since here both ETMs are displaced and there just one]:

$$P_1^{\text{DP total}} = 2\gamma_0^2 \zeta_1^2 \simeq \begin{cases} 190(s/1.3 \text{ mm})^2 \text{ ppm} & \text{spherical,} \\ 190(s/1.0 \text{ mm})^2 \text{ ppm} & \text{MH.} \end{cases} \quad (4.14)$$

These coupling coefficients and parasitic-mode powers are sufficiently small that transverse displacements are not a serious issue, and so shall ignore them in the rest of this paper. In any event, the low sensitivity to a change from fiducial spherical to fiducial MH mirrors makes displacement a non-issue in the any decision about whether to use MH mirrors.

### F. Errors in the Arm Cavities' Mirror Figures

#### 1. Billingsley's Worst-Case Figure Error

Garilynn Billingsley (of the LIGO Laboratory, Caltech) has provided us with a map of a worst-case figure error,  $\delta z_{\text{wc}}(x, y)$  [height error as function of Cartesian coordinates in the transverse plane], produced by current technologies. Her map is based on the measured deviation of a LIGO-I beam-splitter substrate from flatness. The measured substrate had diameter 25 cm; she stretched its deviation from flatness (its "figure map") to the fiducial mirror diameter of 32 cm, fit Zernike polynomials to the stretched map, and smoothed the map by keeping only the lowest 36 Zernikes.

We show a contour diagram of the resulting figure map (figure "error") in Fig. 6. In the central region (innermost 10 cm in radius), the peak to valley error  $\Delta z$  is about 30 nm, while in the outer region (10 cm to 16 cm in radius), it is about 110 nm. Billingsley thinks it likely that in the central region (which dominates our considerations), peak-to-valley errors of  $\Delta z \sim 5$  nm may be achievable for MH mirrors — about 1/5 as large as in Fig. 6; and we have found that  $\Delta z = 0.2 \times 30 = 6$  nm is small enough that the influences of the figure error scale, for  $\Delta z \lesssim 6$  nm, as  $\Delta z$  or  $\Delta z^2$  with higher-order terms producing  $\lesssim 10$  per cent corrections. Accordingly, in the analyses described below we shall use Billingsley's map, scaled down in height by a factor  $\varepsilon$ :

$$\delta z = \varepsilon \delta z_{\text{wc}}(x, y) , \quad (4.15)$$

<sup>9</sup> Here  $\zeta_1^{\text{sph}}$  and  $\zeta_1^{\text{MH}}$  are from R'OS [15] Eqs. (57) and (58). ED'A (unpublished) obtains  $\zeta_1^{\text{MH}} \simeq 0.008 s_{\text{mm}}$ , 20 per cent smaller than R'OS; we regard her  $\zeta_1^{\text{MH}}$  as less reliable than R'OS's because the phase of a parameter  $\gamma_2$  used in her fit is not known with sufficient reliability.

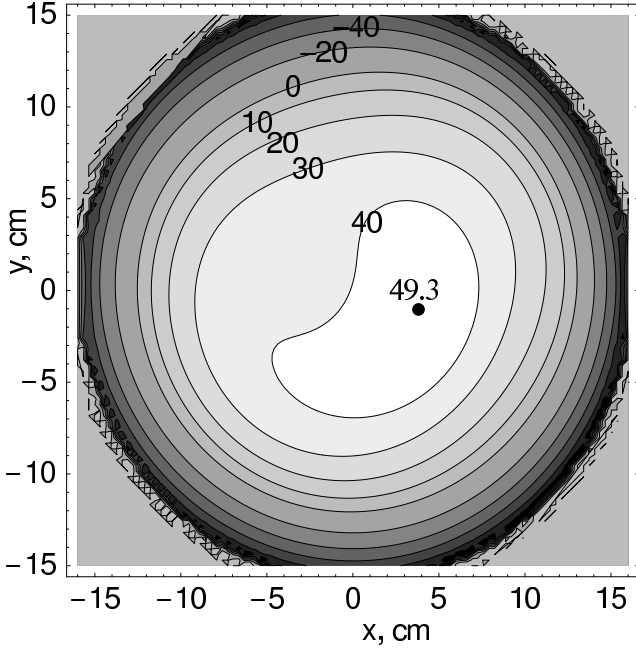


FIG. 6: Contour diagram of Billingsley's worst-case figure error [height  $\delta z_{wc}$  in nanometers as a function of transverse Cartesian coordinates  $(x, y)$  in centimeters]. The hash at the outer edge of the mirror is an artifact of our numerical manipulation of Billingsley's map.

and we shall use  $\varepsilon = 0.2$  and  $\Delta z = 6$  nm as our fiducial values for  $\varepsilon$  and  $\Delta z$ . Jean Marie Mackowski (an expert in coating mirrors) believes that  $\Delta z \sim 2$  nm errors may be achievable for MH mirrors, if the mirror figure is produced by coating; this corresponds to  $\varepsilon \sim 0.07$ . For comparison, the figure errors for the spherical LIGO-I mirrors are  $\Delta z \sim 3$  to 6 nm (rms errors  $\sim 1$  to 2 nm).

## 2. Mode Mixing by Figure Errors Without Compensating Tilt

We have computed the mode mixing in an MH cavity when Billingsley's worst-case figure error, reduced by  $\varepsilon \lesssim 0.2$ , is placed on the ETM. As in our tilt studies, the computation was done independently by ED'A using the FFT code and by RO'S using arm-cavity perturbation theory.

By analogy with Eq. (4.3), the fundamental mode with deformed ETM has the following form

$$u'_0 = (1 - \beta_1^2/2)u_0 + \beta_1 v_1, \quad (4.16)$$

where the parasitic mode  $v_1$ , like the  $u_n$ 's, has unit norm  $\langle v_1 | v_1 \rangle = \int |v_1|^2 d\text{Area} = 1$ , and has its phase adjusted so that  $\beta_1 \propto \varepsilon/0.2$  is real. By contrast with the tilt-induced mode mixing, where  $u_1$  is dipolar (angular dependence  $\cos \varphi$ ), the deformation parasite  $v_1$  has a complicated shape that depends on the details of the deformation and that therefore contains a number of multipoles. A map

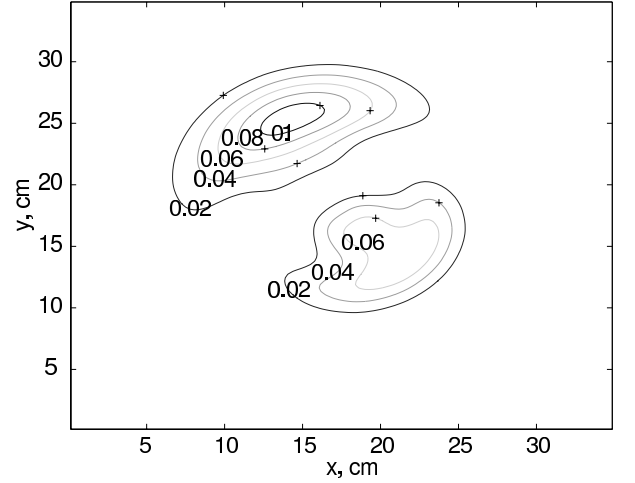


FIG. 7: The power distribution  $|u'_0 - u_0|^2 = |\beta_1 v_1|^2$  (in units  $1/\text{m}^2$ ) of the deformation-induced parasitic mode when the deformation  $\varepsilon \delta z_{wc}(x, y)$  with  $\varepsilon = 0.2$  is applied to the ETM of an MH arm cavity. This map was computed by ED'A [16] using the FFT code; the map computed by RO'S using perturbation theory [15] is in reasonable agreement with this one (e.g., the heights of the two peaks are  $\{0.111, 0.080\}$  in the FFT map, and  $\{0.110, 0.088\}$  in the perturbation map). The parasitic power  $|\beta_1 v_1|^2$  scales as  $(\varepsilon/0.2)^2$ .

of the power distribution  $|\beta_1 v_1|^2$  of the admixed mode is shown in Fig. 7.

The fraction of the arm cavity power in the parasitic mode is

$$P_1^{\text{MH arm}} = \beta_1^2 = 0.0011(\varepsilon/0.2)^2 \quad (4.17)$$

(Eqs. (73) of [15]; first term in first equation on page 10, and also first equation on page 11, of [16]). The fraction of the interferometer's input power that goes out the dark port (if the interferometer is driven by the best-fit Gaussian mode  $u_d$  and if only one of the arm mirrors — one ETM — is deformed) is given by

$$P_1^{\text{MH DP}} = \gamma_0^2 \beta_1^2 = 0.0010(\varepsilon/0.2)^2 \quad (4.18)$$

(Eq. (75) of [15]; cf. also [16]). At the leading,  $\varepsilon^2$ , order in the deformation (the order to which we have computed), this dark-port power is entirely in the parasitic mode  $v_1$ . Our FFT and perturbation-theory calculations agree on the parasitic powers (4.17) and (4.18) to within about five per cent.

The dark-port power (4.18) and parasitic arm-cavity power (4.17) are influenced primarily by the figure error in the central (10 cm radius) region of the ETM, because about 96 per cent of the mesa-mode power is contained in that central region, and only about 4 per cent in the outer region — and of the outer 4 per cent, 3/4 (3 per cent) is in the annulus between 10 and 11 cm. The insensitivity to outer-region deformations is fortunate, because Billingsley tells us that it will be much easier to keep the

figure errors small in the central region than in the outer region.

[We have verified the insensitivity to the outer-region deformations by evaluating (R'OS via perturbation theory and ED'A via FFT simulations) the dark-port power for a mirror deformation of the form

$$\delta z = \epsilon_c \delta z_{wc}^{\text{central}} + \epsilon_o \delta z_{wc}^{\text{outer}}. \quad (4.19)$$

Here  $\delta z_{wc}^{\text{central}}$  is equal to  $\delta z_{wc}$  at  $r < 9.6$  cm and is zero at  $r > 12.2$  cm, and between 9.6 and 12.2 cm,  $\delta z_{wc}^{\text{central}}/\delta z_{wc}$  falls linearly from 1 to zero; and similarly  $\delta z_{wc}^{\text{outer}}$  is equal to  $\delta z_{wc}$  at  $r > 12.2$  cm and is zero at  $r < 9.6$  cm, and between 9.6 and 12.2 cm  $\delta z_{wc}^{\text{outer}}/\delta z_{wc}$  grows linearly from 0 to 1. We find, as a function of the central-region and outer-region weightings,<sup>10</sup>

$$P_1^{\text{MH DP}} = \gamma_0^2 \beta_1^2 \simeq 0.0010[(\epsilon_c/0.2)^2 + (\epsilon_o/0.7)^2]; \quad (4.20)$$

so that, for example, if Billingsley's worst-case perturbations are reduced by  $\epsilon_c = 0.2$  in the central region (to  $\Delta z = 6$  nm), but are reduced only to  $\epsilon_o = 0.7$  in the outer region (so  $\Delta z = 21$  nm there), the outer region will contribute about as much power to the dark port as the inner region.]

When all four arm-cavity mirrors are subjected to uncorrelated deformations, the arm-cavity parasitic power (4.17) will be increased by a factor 2 and the dark-port power (4.18) by a factor 4, to

$$\begin{aligned} P_1^{\text{MH arm total}} &= 2\beta_1^2 \simeq 0.0025(\Delta z/6\text{nm})^2, \\ P_1^{\text{MH DP total}} &= 4\gamma_0^2 \beta_1^2 \simeq 0.005(\Delta z/6\text{nm})^2 \end{aligned} \quad (4.21)$$

where  $\Delta z$  is the peak-to-valley mirror deformation in the central region. This suggests that, so far as arm-cavity mode mixing is concerned, peak-to-valley figure errors of order 6 nm in the inner 10 cm are acceptable.

### 3. Mode Mixing by Figure Errors With Compensating Tilt

The parasitic mode  $v_1$  (Fig. 7) contains a significant amount of dipolar field, as one sees from the asymmetry of the map. The advanced LIGO tilt control system,

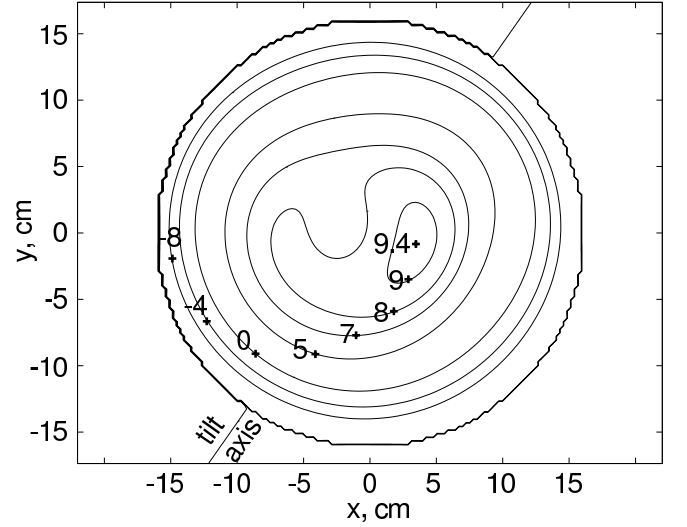


FIG. 8: Billingsley's worst-case figure error reduced by a factor  $\epsilon = 0.2$ , when the mirror is tilted to optimally reduce the mesa beam's odd-parity power:  $\delta z = 0.2\delta z_{wc} + \theta_{\text{compensate}} \sin(\varphi - 55^\circ)$ . The numbers on the contours are height in nanometers.

based on a quadrant-diode readout of asymmetry in the power distribution  $u'_0$ , will tilt the mirror so as to remove the overlap between the deformed parasitic field  $v_1$  and the dipolar-tilt parasitic field  $u_1$ . ED'A and R'OS have independently computed that the optimal tilt is about  $\theta_{\text{compensate}} = 1.3 \times 10^{-8}(\epsilon/0.2)$  radians about a line rotated 55 degrees from the  $x$  axis (Eqs. (77) of [15]), and have computed the resulting field  $u'_0 = u_0 + \beta_1 v_1 + \alpha_1 u_1$  with minimum parasitic-mode power. Figure 8 shows the mirror deformation after tilt, and Fig. 9 shows the parasitic power distribution  $|\beta_1 v_1 + \alpha_1 u_1|^2$  for  $\epsilon = 0.2$ . Notice that the tilt has largely but not completely removed the dipolar asymmetry. Some residual dipolar field remains — that portion whose radial distribution prevents it from being compensated by a tilt.

We denote by  $v_{1c}$  the tilt-compensated parasitic mode and by  $\beta_{1c}$  its (real) amplitude, so  $\beta_{1c} v_{1c} = \beta_1 v_1 + \alpha_1 u_1$ . Then the cavity's eigenmode, with tilt compensation (including the second-order loss of power from  $u_0$ ) is

$$u'_0 = (1 - \beta_{1c}^2/2)u_0 + \beta_{1c} v_{1c}, \quad (4.22)$$

and optimization of the tilt compensation gives for the fraction of the power in the parasitic mode

$$P_{1c}^{\text{MH arm}} = \beta_{1c}^2 = 0.00040(\epsilon/0.2)^2 = 0.00040(\Delta z/6\text{nm})^2 \quad (4.23)$$

(Eq. (79) of [15]; last equation on page 10 of [16], divided by  $\gamma_0^2 = 0.940$ ). The fraction of the interferometer's input power that goes out the dark port (all in the parasitic modes), after this tilt compensation, is

$$P_1^{\text{MH DP}} = \gamma_0^2 \beta_{1c}^2 = 0.00038(\epsilon/0.2)^2 \quad (4.24)$$

(Eq. (80) of [15]; last equation on page 10 of [16]).

<sup>10</sup> The second coefficient,  $(\epsilon_o/0.7)^2$ , is from the ED'A FFT calculations: a fit to numbers in the first and third equations on page 11 of [16], in which fit we (arbitrarily) ignored the possibility of a cross term between  $\epsilon_o$  and  $\epsilon_c$ . The RO'S perturbation-theory calculations use mirrors of infinite radius, and the modes admixed by the outer-region perturbations have sufficient amplitude outside the radius of our fiducial mirror,  $r > 16$  cm, as to make his results for the dependence on  $\epsilon_o$  somewhat unreliable. (The unreliability arises from two effects: his admixed modes are wrong due to omitting the influence of the mirror edge, and his analysis misses the influence of the mirror errors on diffraction losses.) His analog of Eq. (4.20) is  $P_1^{\text{MH DP}} \simeq 0.0010[(\epsilon_c/0.2)^2 + \epsilon_o(\epsilon_o - \epsilon_c)/(0.7)^2]$ , implying 5 times weaker sensitivity to outer-region perturbations than central-region, by contrast with the 3.5 times weaker sensitivity in ED'A's more reliable Eq. (4.20).



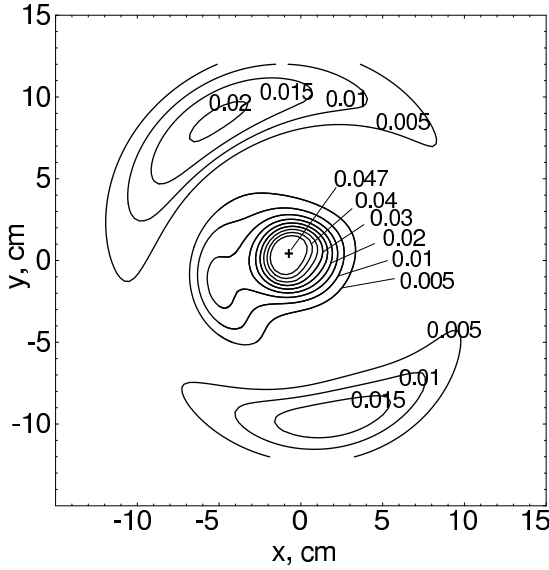


FIG. 9: The power distribution  $|u'_0 - u_0|^2 = |\beta_{1c} v_{1c}|^2$  (in units  $1/\text{m}^2$ ) of the deformation-induced parasitic mode when the tilt-adjusted deformation  $\delta z = 0.2\delta z_{\text{wc}} + \theta_{\text{compensate}} \sin(\varphi - 55^\circ)$  is applied to the ETM of an MH arm cavity. This map was computed by RO'S by applying perturbation theory to the cavity's eigenmode [15]. The map computed by ED'A using the FFT code [16] agrees reasonably well.

Comparing with Eq. (4.18), we see that *the figure-error-induced power out the dark port is reduced by a factor 3 by the compensating tilt of the deformed mirror.*

The dark-port power (4.24) is for an interferometer with one deformed MH arm mirror. When all four mirrors are deformed in uncorrelated ways, the arm-cavity parasitic power will be doubled and the dark-port power will be quadrupled:

$$\begin{aligned} P_1^{\text{MH arm total}} &= 2\beta_{1c}^2 \simeq 0.0008(\Delta z/6\text{nm})^2, \\ P_1^{\text{MH DP total}} &= 4\gamma_0^2\beta_{1c}^2 \simeq 0.0015(\Delta z/6\text{nm})^2 \quad (4.25) \end{aligned}$$

*This suggests that, so far as arm-cavity mode mixing is concerned, we could live with central-region deformations as large as 10 nm. Recycling-cavity issues, discussed below, will place much tighter constraints on the mirror figures.*

We note in passing that the computations reported in this subsection have verified the ability of the LIGO control system to measure the lowest-radial-order dipolar component of a mirror figure error, and remove it by applying a tilt.

#### 4. Comparison with Mode Mixing for Baseline Spherical Mirrors with Tilt-Compensated Figure Errors

As part of her modeling of the baseline configuration of advanced LIGO (a different project from that reported here), Ed'A has evaluated tilt compensation and

mode mixing for an interferometer with the baseline (BL) spherical mirrors, to which the figure error of Fig. 6 with  $\varepsilon = 0.2$  has been applied. For the BL spherical mirrors, 95 per cent of the light power is contained inside a circle with radius  $r_{95\%} \simeq 7.3$  cm, by contrast with the fiducial MH mirrors, where  $r_{95\%} \simeq 10$  cm (and the fiducial spherical mirrors with  $r_{95\%} \simeq 8$  cm). Since  $(7.3/10)^2 \simeq 0.5$ , the BL Gaussian beam feels a central region of the deformed mirror with area approximately half that felt by the fiducial mesa beam.

Interestingly, the tilt compensation that removes the lowest-radial-order dipolar deformation is twice as large for the BL spherical case as for the fiducial MH case:  $\theta_{\text{compensate}}^{\text{BL sph}} \simeq 2.6 \times 10^{-8}(\varepsilon/0.2)$  compared to  $\theta_{\text{compensate}}^{\text{fid MH}} \simeq 1.3 \times 10^{-8}(\varepsilon/0.2)$ . The BL tilt is about a line rotated 76 degrees from the  $x$ -axis, compared to 55 degrees for the fiducial MH case. These differences are due to the different regions of the mirror that the two beams feel.

After tilt compensation, the peak-to-valley figure-error variations in the 95-per-cent-power region are [for figure errors reduced from worst case by  $\varepsilon = 0.2$ ]  $(\Delta z)_{95\%}^{\text{BL sph}} \simeq 2$  nm (inner 7.3 cm), by contrast with  $(\Delta z)_{95\%}^{\text{fid MH}} \simeq 6$  nm (inner 10 cm). This factor 3 difference is caused by Billingsley's figure errors becoming larger rapidly with increasing radius — an issue that will have to be dealt with if MH mirrors are used in advanced LIGO.

D'Ambrosio's analysis of mode mixing by the tilt-compensated figure errors gives, for the fraction of arm-cavity power driven into parasitic modes,  $P_1^{\text{BL sph arm total}} \simeq 0.0008[(\Delta z)_{95\%}/12\text{nm}]^2$ , compared to  $P_1^{\text{MH arm total}} \simeq 0.0008[(\Delta z)_{95\%}/6\text{nm}]^2$  [Eq. (4.25)]. Thus, for the same amount of mode mixing, the BL spherical mirrors can have twice as large peak-to-valley figure errors as the fiducial MH mirrors, and in the BL spherical case the relevant figure errors are confined to a region half as large in area ( $r_{95\%} \simeq 7.3$  cm) as in the fiducial MH case ( $r_{95\%} \simeq 10$  cm). Presumably, the two-fold greater sensitivity of MH arm cavities to figure errors is caused by the greater degeneracy of their modes (last paragraph of Sec. IV C). If we had compared fiducial MH mirrors with fiducial spherical mirrors instead of with BL spherical mirrors, the differences would have been more modest.

#### G. Influence of Mirror Tilt and Figure Errors on Thermoelastic Noise

When one MH mirror of an arm cavity is given the deformation  $\varepsilon\delta z_{\text{wc}}$ , the resulting deformation of the arm-cavity power distribution,  $\delta|u'_0|^2 = |u'_0|^2 - |u_0|^2$  increases the thermoelastic noise. The following argument (due to RO'S Secs. IV C 4 and VII E 4 of [15]) shows that, at leading (linear) order in  $\varepsilon/0.2$ , *only the circularly symmetric portion of the parasitic mode  $\beta_{1c} v_{1c} = u'_0 - u_0$  contributes to the thermoelastic noise increase*: The fractional noise increase is equal to the fractional increase in the ther-

moelastic noise integral  $I = \int (\vec{\nabla}\Theta)^2 d\text{volume}$  [Eqs. (3.1) and (3.2)]:

$$\frac{\delta S_h^{\text{TE MH}}}{S_h^{\text{TE MH}}} = \frac{\delta \bar{I}}{\bar{I}} \propto \int (\vec{\nabla}\Theta) \cdot (\vec{\nabla}\delta\Theta) d\text{volume}. \quad (4.26)$$

Here  $\Theta$  is not a tilt angle but rather is the expansion (fractional increase of volume) of the substrate material when a static pressure  $P \propto |u'_0|^2$  is applied to the mirror face. Since the unperturbed mesa beam is circularly symmetric, so will be the unperturbed expansion  $\Theta$ , which means that only the circularly symmetric portion of the expansion perturbation  $\delta\Theta$ , and thence the circularly symmetric portion of the pressure perturbation  $\delta P \propto \delta|u'_0|^2$  will contribute to the noise increase. At leading (linear) order in the mirror deformation  $\varepsilon/0.2$ , the circularly symmetric portion of  $\delta|u'_0|^2$  arises solely from the circularly symmetric portion of  $\delta u'_0 = \beta_1 v_1$ ; thus, as claimed, only the circularly symmetric portion of  $\beta_1 v_1$  can increase the thermoelastic noise.

This same argument shows that *the mesa-mode deformation produced by mirror tilt cannot influence the thermoelastic noise at first order in the tilt angle; and therefore, we need not be concerned about the influence of tilt on the thermoelastic noise — whether the tilt is unintended, or is being used in a controlled way to compensate the errors in the mirror figures.*

RO'S and SS have independently computed the fractional increase in the thermoelastic noise integral at linear order in  $\varepsilon/0.2$ ; cf. Eq. (81) in OSV [15]. Their result, multiplied by four to account for four arm-cavity mirrors, is

$$\frac{\delta S_h^{\text{TE, MH total}}}{S_h^{\text{TE, MH}}} = 0.14(\varepsilon/0.2) \simeq 0.14(\Delta z/6\text{nm}). \quad (4.27)$$

*This 14 per cent increase of  $S_h$ , when all four mirrors are subjected to 6 nm figure errors in their central regions, is to be compared with the factor  $1/0.34 = 295$  per cent decrease in thermoelastic noise achieved by switching from spherical mirrors to MH mirrors. There may also be a small increase in thermoelastic noise when a spherical mirror is deformed. Assuming, conservatively, no deformation-induced noise increase for spherical mirrors, switching from spherical to 6nm-deformed MH mirrors will reduce the thermoelastic noise by a factor  $0.34 \times 1.14 = 0.39$ , which in turn will increase the distance for NS/NS binaries from 364 Mpc to about 490 Mpc (Fig. 4) and increase the event rate by about a factor 2.45; cf. Table I.*

## H. Mesa vs. Gaussian Beams in Recycling Cavities

In LIGO-I interferometers, and in the baseline design for advanced LIGO interferometers, the greatest sensitivity to mirror tilts and figure errors occurs in the power recycling (PR) and signal recycling (SR) cavities. This sensitivity arises from the near degeneracy of the recycling

cavities, which strongly enhances error-induced mode mixing. One might worry that for MH mirrors, with their greater central-region flatness, this severe mode mixing might be made substantially worse.

We have examined this question and conclude that *for the two wideband advanced LIGO interferometers, there is not much difference between the fiducial Gaussian beams and the fiducial mesa beams, with regard to their susceptibility to mode mixing in the recycling cavities.* The only significant difference arises from the fact that the mesa beams are larger and therefore sample, with significant power, larger-radii regions of the mirrors (the regions between, say, 8 cm radius and 10 cm radius), where the deformations may be worse.

The reason that the mode mixing is only marginally sensitive to the beam shape is quite simple: If heterodyne readout were used, then once RF modulated sideband light gets into the RF optical cavity bounded by the power recycling (PR) mirror, the signal recycling (SR) mirror and the two input test-mass (ITM) mirrors, the sideband light would make roughly  $\mathcal{N}_{\text{RF}} \sim \frac{1}{2}(\text{cavity finesse } \mathcal{F}_{\text{PR}}) \simeq (\pi/2)/(1 - R_{\text{PR}}) \simeq 25$  round trips before losing 95 per cent of its power out the beam splitter's dark port.<sup>11</sup> (Here  $R_{\text{PR}} = R_{\text{SR}} \simeq 0.94$  is the power reflectivity of the PR and SR mirrors; they are made equal so as to transmit the RF light with maximum efficiency to the photodetector.) And once signal light gets into the signal recycling cavity, it makes roughly  $\mathcal{N}_{\text{SR}} \sim \frac{1}{2}\pi/(1 - \rho\sqrt{R}) \sim 40$  round trips before losing 95 per cent of its power out the dark port or back into the arm cavities. (Here  $R = 0.995$  is the ITM power reflectivity and  $\rho = \sqrt{0.93}$  is the amplitude reflectivity of the SR mirror, in the notation of Buonanno and Chen [9].) The Fresnel length (transverse diffraction scale) for light that makes  $\mathcal{N}$  round trips in either recycling cavity, with cavity lengths  $\ell_{\text{RF}} \simeq 20$  m and  $\ell_{\text{SR}} \simeq 10$  m, is

$$r_F = \sqrt{\lambda_o 2\ell\mathcal{N}} \simeq 3\text{cm}, \quad (4.28)$$

for both cavities; here  $\lambda_o = 1\mu\text{m}$  is the light's wavelength. This Fresnel length is  $\sim 1/2$  of the  $\sim 5$  cm scales on which the ideal mirror shapes and the central-region worst-case mirror errors vary, and it is small compared to the  $\sim 15$  to 20 cm diameter beams themselves. There thus is only modest diffractive coupling between light rays, and *the light bouncing back and forth in each recycling cavity is describable, to moderately good accuracy, by geometric optics.* Moreover, because the mirrors (whether MH or spherical) are nearly flat and nearly identical, the light's rays, to rather good accuracy, are all parallel to the optic axis and to each other and are thus decoupled from each other. If the mirrors and beam splitter were perfect and

<sup>11</sup> Our definition  $\mathcal{N} = (\text{number of round trips}) \simeq \mathcal{F}/2$ , based on 95 per cent power loss, differs by  $4/\pi \simeq 1.27$  from a more conventional  $\mathcal{N} = (2/\pi)\mathcal{F}$  based on the phase shift of light emerging from the cavity.

ideal in shape, the extreme length of their radii of curvature,  $\gtrsim 50$  km, compared to the optical pathlength in the recycling cavities,  $2\ell\mathcal{N} \simeq 1$  km, would guarantee that the mesa beam would resonate equally well in the ideal MH-mirrored cavity or in the ideal spherical-mirrored cavity, or in a precisely flat-mirrored cavity; and the fiducial Gaussian beam would also resonate, equally well, in all these cavities.

If an advanced LIGO interferometer is operated in narrow-band mode, then the number of round trips the signal light makes in the SR cavity will be much larger than 40, and the geometric optics approximation will begin to fail significantly. More specifically, for ITM reflectivity  $R = 0.995$  and optimized narrow banding at  $\{500 \text{ Hz}, 1000 \text{ Hz}\}$ , the SR mirror's amplitude reflectivities are  $\rho = \{0.994, 0.9985\}$  [see discussion following Eq. (4.35) below], corresponding to a number of round trips in the SR cavity  $\mathcal{N}_{\text{SR}} \simeq \{180, 400\}$  and Fresnel lengths  $r_F \simeq \{6 \text{ cm}, 9 \text{ cm}\}$ . These Fresnel lengths (the transverse scale for diffractive light spreading) are about 1/3 to 1/2 the 95-percent-power diameter of the beam, 16 cm (fiducial Gaussian) and 20 cm (fiducial mesa). As we shall see below, this means that geometric optics can be used to get a rough upper limit on the fractional decrease of signal strength due to tilt and irregularities of the SR cavity's mirrors.

## I. Decrease of Signal Strength Due to Mirror Tilts

### 1. Foundations

The mirror tilts produce a mismatch between various modes of the light, thereby decreasing the signal strength at the interferometer output (the beam splitter). We shall focus on the signal-strength decrease at the frequency of the signal light's optical resonance in the arm cavity. This optical resonance is the one that is used to produce a noise  $[S_h(f)]$  minimum for a narrowbanded advanced LIGO interferometer, and it is the right-hand minimum (at  $f \simeq 230$  Hz) of the optical noise for the standard wide-band advanced LIGO interferometer (Fig. 1), and approximately the minimum of the wide-band interferometer's total noise. At this frequency, for MH mirrors with their reduced thermoelastic noise, the dominant noise source is shot noise; for spherical mirrors, short noise and thermoelastic noise are comparable at this frequency, but in a small piece of our analysis, we shall idealize the shot noise as dominant.

The (unit-norm) modes whose mismatch decreases the signal strength are the following:

1.  $u_0$ , the eigenmode of perfect arm cavities.
2.  $u'_0$ , the carrier's eigenmode in an arm cavity with tilted ITM and ETM.
3.  $u'_s$ , the signal field's eigenmode in an arm cavity, at the center of its optical resonance, with tilted ITM,

ETM, and SRM (signal recycling mirror).

4.  $u'_t$ , the field produced when  $u_0$  is transmitted through the signal recycling cavity with tilted ITM and SRM.
5.  $u'_r$ , the reference-light field that is beat against the signal light to produce the input to the photodetector. For the baseline homodyne readout system, this will be carrier light  $u'_0$  transmitted through the ITM and SR mirror to the photodiode. If heterodyne readout were used, it would be side-band light transmitted through the RF cavity to the photodetector.

For each primed field  $u'_\ell$ , we denote by  $\delta_\ell$  the fraction of its light power that is in parasitic modes and thus has been lost from the fundamental mode  $u_0$  due to mirror tilt:

$$\langle u_0, u'_\ell \rangle^2 = 1 - \delta_\ell. \quad (4.29)$$

The signal amplitude entering the photodetector is proportional to

$$S \propto \langle u'_r, \tilde{\tau}' u'_s \rangle \langle u'_s, u'_0 \rangle \langle u'_0, u_d \rangle. \quad (4.30)$$

The sequence of terms, from right to left, have the following meanings, and we approximate them as follows:

1.  $\langle u'_0, u_d \rangle$  describes the influence of tilts on the driving of the arm cavity's eigenmode by the Gaussian driving field. For simplicity, we neglect the tiny coupling of the driving field to the second-order parasitic mode  $u_2$  contained in  $u_0$  and therefore approximate this coupling amplitude by  $\langle u'_0, u_d \rangle = \gamma_0 \langle u'_0, u_0 \rangle = \gamma_0 (1 - \alpha_{1E}^2/2 - \alpha_{1I}^2/2) = \gamma_0 (1 - \delta_0/2)$ . Here the subscripts  $I$  and  $E$  denote the contributions from the tilts of the ITM and ETM.
2.  $\langle u'_s, u'_0 \rangle$  describes the influence of tilts on the driving of the arm cavity's signal field by its carrier field (via the gravitational-wave-induced motion of the mirrors). For simplicity we neglect the (nonzero) overlap between the parasitic modes contained in  $u'_s$  and  $u'_0$ , thereby obtaining  $\langle u'_s, u'_0 \rangle = (1 - \delta_s/2 - \delta_0/2)$ .
3.  $\langle u'_r, \tilde{\tau}' u'_s \rangle$  describes the influence of tilts on (i) the passage of the signal  $u'_s$ , through the SR cavity (with cavity transmissivity  $\tilde{\tau}'$  in the notation of Buonanno and Chen [9]), and on (ii) the overlap of the transmitted signal light with the reference light to produce the photodetector current. Again we neglect correlations between the parasitic components of the fields and therefore approximate the influence of the tilts by  $\langle u'_r, \tilde{\tau}' u'_s \rangle \propto (1 - \delta_r/2 - \delta_s/2 - \delta_t/2)$ . The  $\delta_j$  terms represent the loss of overlap due to the parasitic-mode fields (assumed uncorrelated) contained in  $u'_r$  (the  $\delta_r$  term), contained in  $u'_s$  (the  $\delta_s$  term), and generated by

the passage of the signal light through the SR cavity, whose mirror tilts deform the transmissivity  $\tilde{\tau}'$ , (the  $\delta_t$  term).

If there is no mode cleaner on the interferometer output, then the rms amplitude of the shot noise (the dominant noise source at our chosen frequency) is  $N \propto \sqrt{\langle u_r', u_r' \rangle} = 1$ ; i.e. the parasitic-mode components of  $u_r'$  contribute to the rms noise amplitude along with the fundamental-mode component. However, a mode cleaner will remove the parasitic components, so that  $N \propto \langle u_0, u_r' \rangle = 1 - \delta_r/2$ .

Combining the above approximations to the various terms, we find for the ratio of noise power to signal power (which is proportional to the spectral density of noise  $S_h$  referred to the gravitational-wave input  $h$ ), at the minimum of the optical resonance:

$$S_h \propto \frac{N^2}{|S|^2} \propto 1 + 2\delta_0 + 2\delta_s + \delta_t + \begin{cases} \delta_r, & \text{no mode cleaner} \\ 0 & \text{with mode cleaner.} \end{cases} \quad (4.31)$$

(Note that we have ignored the increase in shot noise due to carrier-light parasitic fields going out the dark port, Eqs. (4.9) and (4.25), under the assumption that it is negligible, either because of an output mode cleaner or because the arm-cavity-mirror figures and tilts are adequately controlled.)

We shall now examine the various contributions to the increase of  $S_h$  one by one.

## 2. Carrier Light in Arm Cavity

The fraction of the arm-cavity carrier power that is driven into parasitic modes by tilts of the ETM and ITM is  $\delta_0 = \alpha_{1E}^2 + \alpha_{1I}^2$ . The loss of this carrier power to parasites reduces the signal power  $S^2$  and thence increases the gravitational-wave noise by

$$\left( \frac{\delta S_h}{S_h} \right)_{\text{carrier}}^{\text{MH}} = 2\delta_0 = 4\alpha_1^2 = 0.01 \left( \frac{\theta}{2 \times 10^{-8}} \right)^2. \quad (4.32)$$

Here we have assumed that both mirrors are tilted through the same angle  $\theta$  but about uncorrelated axes, we have assumed MH mirrors, and we have used Eq. (4.5) for  $\alpha_1$ . The fiducial spherical mirrors are four times less sensitive to tilt, so to keep this contribution to  $S_h$  below one per cent, we must control the ITM and ETM tilts to an accuracy

$$\theta_{1\%}^{\text{MH}} = 2 \times 10^{-8}, \quad \theta_{1\%}^{\text{sph}} = 8 \times 10^{-8}. \quad (4.33)$$

These are modest constraints on tilt.

## 3. Signal Light in Arm Cavity

The signal recycling (SR) cavity presents a complex amplitude reflectivity  $\tilde{\rho}' = e^{-\epsilon/F} e^{i\lambda/F}$  to the arm cavity's signal light (Eqs. (5) and (13) of Buonanno and

Chen [9]). Here  $F = c/2L$  is the interferometer's free spectral range,  $\epsilon = \epsilon(R, \rho, \phi)$  and  $\lambda = \lambda(R, \rho, \phi)$  are real functions of the ITM power reflectivity  $R$ , the SRM amplitude reflectivity  $\rho$  and the SR cavity's tuning phase  $\phi = (k\ell)_{\text{mod } 2\pi}$ , with  $\ell$  the length of the cavity; and our notation is that of Buonanno and Chen [9]. Tilts of the ITM and SRM produce a spatially variable reflectivity  $\tilde{\rho}'$ . The spatial variations of the modulus  $e^{-\epsilon/F}$  of  $\tilde{\rho}'$  presumably will have much less influence on the arm cavity's signal eigenmode  $u_s'$  than the spatial variations of the phase. (This claim deserves to be checked.) Assuming this is so, then the dominant influence of an ITM or SRM tilt  $\theta$  is to produce a spatially variable mirror displacement

$$\delta z = \theta r \sin \varphi \quad (4.34)$$

(where  $\varphi$  is azimuthal angle and  $r$  is radius), which in turn (*in the SR cavity's geometric optics limit*) produces a spatially variable phase of the cavity reflectivity,  $\arg(\tilde{\rho}') = \delta\lambda/F = (d\lambda/d\phi)(k/F)\delta z$ . If the cavity were replaced by a single mirror that is displaced through a distance  $\delta z_{\text{eff}}$ , then this phase change would be  $2k\delta z_{\text{eff}}$ . Correspondingly, the tilt of the ITM or SRM produces an effective mirror displacement  $\delta z_{\text{eff}} = \mathcal{A}\delta z$ , where the amplification factor  $\mathcal{A}$  is given by

$$\mathcal{A} = \frac{\delta z_{\text{eff}}}{\delta z} = \frac{d\lambda/d\phi}{2F} = (1-R)\rho \frac{2\rho + (1+\rho^2)\cos 2\phi}{(1+\rho^2) + 2\rho\cos 2\phi}; \quad (4.35)$$

see Eq. (18) of Buonanno and Chen [9].

We shall focus on three configurations for the SR cavity: (i) The standard wideband advanced LIGO configuration (denoted “WB”), for which  $R = 0.995$ ,  $\rho = \sqrt{0.93}$ , and  $\phi = \pi/2 - 0.06$ . (ii) An interferometer narrowbanded at a frequency  $f = \lambda/2\pi \simeq 500$  Hz with bandwidth  $\Delta f = \epsilon/2\pi \simeq 50$  Hz, which has a noise minimum of  $\simeq 1 \times 10^{-24}/\sqrt{\text{Hz}}$ ; this configuration (which we shall denote “500”) is produced by  $R = 0.995$ ,  $\rho = 0.994$ , and  $\phi = 1.541$ . (iii) An interferometer narrowbanded at  $f = \lambda/2\pi \simeq 1000$  Hz with bandwidth  $\Delta f = \epsilon/2\pi \simeq 50$  Hz (and so denoted “1000”), which has a noise minimum of  $\simeq 1 \times 10^{-24}/\sqrt{\text{Hz}}$  and parameters  $R = 0.995$ ,  $\rho = 0.9985$ ,  $\phi = 1.556$ . For these three configurations the amplification factor is

$$\mathcal{A}_{\text{WB}} = 0.27, \quad \mathcal{A}_{500} = 1.4, \quad \mathcal{A}_{1000} = 5.7. \quad (4.36)$$

We have chosen to compute the signal loss at the optical resonance so the signal field  $u_s'$  in the arm cavity will be on resonance, just as the carrier field is. This allows us to translate our carrier-field results over to the signal field with only one change: the influence of the tilts of the SRM and ITM must be multiplied by the amplification factor  $\mathcal{A}$ . Therefore, the fraction  $\delta_s$  of the signal field's power that is in the tilt-induced parasitic modes is  $\delta_s = \alpha_{1E}^2 + \mathcal{A}^2(\alpha_{1I}^2 + \alpha_{1SR}^2)$ . The influence  $\alpha_{1E}^2$  of the ETM is the same as in the case of the carrier, which we have already dealt with, so we shall ignore it here and focus on the two mirrors that make up the SR cavity: the

ITM and the SRM. If they both have the same tilt angles  $\theta$  (but about uncorrelated axes) so  $\alpha_{1I}^2 = \alpha_{1SR}^2 \equiv \alpha_1^2$ , then these tilts produce a fractional loss of signal power and hence fractional increase in gravitational-wave noise given by

$$\left(\frac{\delta S_h}{S_h}\right)_{\text{signal}} = 2\delta_s = 4\mathcal{A}^2\alpha_1^2. \quad (4.37)$$

This is greater by the factor  $\mathcal{A}^2$  than the noise (4.32) due to loss of carrier light into parasitic modes, and correspondingly to keep this fractional increase of  $S_h$  below one per cent requires controlling the ITM and SRM tilts to an accuracy  $1/\mathcal{A}$  of that in Eq. (4.33):

$$\begin{aligned} \theta_{1\%}^{\text{MH WB}} &= 7 \times 10^{-8}, & \theta_{1\%}^{\text{sph WB}} &= 30 \times 10^{-8}, \\ \theta_{1\%}^{\text{MH 500}} &\gtrsim 1.4 \times 10^{-8}, & \theta_{1\%}^{\text{sph 500}} &\gtrsim 6 \times 10^{-8}, \\ \theta_{1\%}^{\text{MH 1000}} &\gtrsim 0.4 \times 10^{-8}, & \theta_{1\%}^{\text{sph 1000}} &\gtrsim 1.4 \times 10^{-8}. \end{aligned} \quad (4.38)$$

For the narrowbanded interferometers these limits are only lower bounds on  $\theta_{1\%}$  because of the failure of the geometric optics limit. As we have seen, the Fresnel length for light trapped in the SR cavity is about 1/2 to 1/3 of the 95-percent-power beam diameter, so transverse spreading of the light will reduce somewhat the SR cavity's amplification factor  $\mathcal{A}$  and hence the influence of tilt on the beam asymmetry. We *guess* that this reduction might increase  $\theta_{1\%}^{1000}$  by a factor of order 2 over the geometric-optics limit, Eq. (4.38); but since  $\mathcal{A}$  is only about 1 for  $\theta_{1\%}^{500}$ , we *guess* that there is little increase in  $\theta_{1\%}^{500}$ ; so

$$\begin{aligned} \theta_{1\%}^{\text{MH 500}} &\simeq 1.4 \times 10^{-8}, & \theta_{1\%}^{\text{sph 500}} &\simeq 6 \times 10^{-8}, \\ \theta_{1\%}^{\text{MH 1000}} &\simeq 0.8 \times 10^{-8}, & \theta_{1\%}^{\text{sph 1000}} &\simeq 3 \times 10^{-8}. \end{aligned} \quad (4.39)$$

#### 4. Transmission of Signal Light Through SR Cavity

When the ITM or SRM is tilted through an angle  $\theta$ , producing a spatially dependent mirror displacement  $\delta z = \theta r \sin \varphi$ , it alters the SR cavity's transmissivity by a spatially dependent amount  $\delta\tilde{\tau}' = (d\tilde{\tau}'/d\phi)k\delta z$ , *in the geometric optics limit*. When an undistorted signal beam  $u_0$  passes through this spatially variable transmissivity, a fraction

$$\langle u_0, |\delta\tilde{\tau}'/\tilde{\tau}'|^2 u_0 \rangle = \frac{1}{2} \mathcal{B}^2 k^2 \langle r^2 \rangle \theta^2. \quad (4.40)$$

gets transferred to parasitic modes. Here  $k = 2\pi/\lambda_o$  is the wave number,  $\langle r^2 \rangle = \langle u_0, r^2 u_0 \rangle$  is the beam's mean square radius, which has the values

$$\begin{aligned} \langle r^2 \rangle &= (6.95\text{cm})^2 && \text{for fiducial mesa beam} \\ \langle r^2 \rangle &= r_o^2 = (4.70\text{cm})^2 && \text{for fiducial Gaussian beam,} \end{aligned} \quad (4.41)$$

and

$$\mathcal{B}^2 = \left| \frac{d\tilde{\tau}'/d\phi}{\tilde{\tau}'} \right|^2 = \frac{4R\rho^2}{1 + R\rho^2 + 2\sqrt{R\rho} \cos 2\phi}. \quad (4.42)$$

Here we have used Eq. (11) of Buonanno and Chen [9] for  $\tilde{\tau}'$ , with the factor  $e^{i\phi(\vec{r})}$  in the numerator removed, so as to obtain the transmissivity that carries the field from an input transverse plane to an output transverse plane in the presence of the mirror tilt (which gives  $\phi$  its dependence on transverse position  $\vec{r}$ ). For our three interferometer configurations, the values of  $\mathcal{B}$  are

$$\mathcal{B}_{\text{WB}} = 15, \quad \mathcal{B}_{500} = 33, \quad \mathcal{B}_{1000} = 66. \quad (4.43)$$

When both ITM and SRM are tilted through the same angle  $\theta$  about uncorrelated axes, the total power transferred into parasitic modes is twice as large as Eq. (4.40) [i.e.,  $\delta_t$  is twice (4.40)], and correspondingly the fractional increase of gravitational wave noise (due to both loss of signal power and increase of shot noise) is

$$\left(\frac{\delta S_h}{S_h}\right)_{\text{transmission}} = \delta_t = \mathcal{B}^2 k^2 \langle r^2 \rangle \theta^2. \quad (4.44)$$

Inserting the above values for  $\mathcal{B}$  and  $\langle r^2 \rangle$  and insisting that  $S_h$  not increase by more than one per cent, we obtain the following constraints on the ITM and SRM tilt angles:

$$\begin{aligned} \theta_{1\%}^{\text{MH WB}} &= 1.6 \times 10^{-8}, & \theta_{1\%}^{\text{sph WB}} &= 2.4 \times 10^{-8}, \\ \theta_{1\%}^{\text{MH 500}} &\gtrsim 0.7 \times 10^{-8}, & \theta_{1\%}^{\text{sph 500}} &\gtrsim 1.1 \times 10^{-8}, \\ \theta_{1\%}^{\text{MH 1000}} &\gtrsim 0.4 \times 10^{-8}; & \theta_{1\%}^{\text{sph 1000}} &\gtrsim 0.6 \times 10^{-8}. \end{aligned} \quad (4.45)$$

For the narrowbanded interferometers, the failure of the geometric optics limit dictates that these estimates of  $\theta_{1\%}$  are lower limits; hence the “ $\gtrsim$ ”. As in the case of signal light in an arm cavity reflecting off the SR cavity, so also here, we *guess* that these estimates are fairly good for narrow banding at 500 Hz and are roughly a factor 2 too severe at 1000 Hz, so

$$\begin{aligned} \theta_{1\%}^{\text{MH 500}} &\simeq 0.7 \times 10^{-8}, & \theta_{1\%}^{\text{sph 500}} &\simeq 1.1 \times 10^{-8}, \\ \theta_{1\%}^{\text{MH 1000}} &\simeq 0.7 \times 10^{-8}; & \theta_{1\%}^{\text{sph 1000}} &\simeq 1.1 \times 10^{-8}. \end{aligned} \quad (4.46)$$

Equations (4.45) for wideband interferometers and (4.46) for narrowband [and (4.39) for  $\theta_{1\%}^{\text{MH 1000}}$ ] are the most severe of all our tilt constraints.

#### 5. Reference light for baseline readout

The baseline design for the advanced LIGO interferometers includes an output mode cleaner and homodyne readout. As we have seen [Eq. (4.31)], the mode cleaner makes  $S_h$  insensitive to (first-order) losses of reference power into parasitic modes.

### 6. Transmission of RF reference light through a power recycling cavity without an output mode cleaner

In LIGO-I interferometers, by contrast with the baseline design of advanced LIGO, there is no output mode cleaner, and heterodyne readout is used in place of homodyne; i.e., the reference light is radio-frequency (RF) sidebands, transmitted to the output port via the RF cavity (which is the same as the power recycling cavity since LIGO-I has no SR mirror). In this section we shall compare our approximate analysis with more careful analyses of LIGO-I, by analyzing this type of readout.

Suppose that the PRM or ITM is tilted through an angle  $\theta$  and is thereby given the space-dependent displacement  $\delta z = \theta r \sin \varphi$ . Then, in the geometric optics limit, the RF reference light acquires, when passing through the PR cavity, a space-dependent phase shift  $(\mathcal{F}/\pi)k2\delta z$ ,<sup>12</sup> where  $\mathcal{F}$  is the cavity finesse. The reference light emerging from the cavity therefore has the form  $u'_r = u_0 e^{i(\mathcal{F}/\pi)k\delta z}$ , for which the fraction of light power in parasitic modes is

$$\left\langle u_0, \left( \frac{2\mathcal{F}}{\pi} \right)^2 k^2 \delta z^2 u_0 \right\rangle = \frac{1}{2} \left( \frac{2\mathcal{F}}{\pi} k \right)^2 \langle r^2 \rangle \theta^2. \quad (4.47)$$

When both the PRM and the ITM are tilted through the same angle  $\theta$  but around uncorrelated axes, the parasitic mode power is twice as large [so  $\delta_r$  is twice (4.47)], and the fractional decrease of signal power, and corresponding increase of gravity-wave noise, due to the loss of this reference-light power, are then

$$\left( \frac{\delta S_h}{S_h} \right)_{\text{reference}} = \delta_r = \left( \frac{2\mathcal{F}}{\pi} k \right)^2 \langle r^2 \rangle \theta^2. \quad (4.48)$$

For the LIGO-I interferometers  $\mathcal{F}$  is rather large,  $\mathcal{F} \simeq 105$ , which produces a strong sensitivity to mirror tilt. By contrast, for advanced LIGO  $\mathcal{F}$  is smaller,  $\mathcal{F} \simeq 50$ , which (as we shall see) compensates for the larger beam. The result would be about the same sensitivity to tilt as for LIGO-I, if there were no output mode cleaner in advanced LIGO and heterodyne readout were used.

Inserting the LIGO-I finesse  $\mathcal{F} \simeq 105$  and mean square beam radius<sup>13</sup>  $\langle r^2 \rangle = b^2 = (2.9\text{cm})^2$ , and constraining the increase of  $S_h$  to less than one per cent, we obtain the following constraint on the ITM and PRM tilts:

$$\theta_{1\%}^{\text{LIGO-I}} \simeq 0.9 \times 10^{-8}. \quad (4.49)$$

This differs by a factor  $\simeq 1.5$  from the result of a much more careful computation by Fritschel et. al. [17], which

gave<sup>14</sup>  $\theta_{1\%}^{\text{LIGO-I}} = 1.4 \times 10^{-8}$ .

If advanced LIGO were to use an RF readout and no mode cleaner, the RF cavity would be bounded by the PR, SR, and ITM mirrors (with each round trip of light encountering the ITM twice). Uncorrelated tilts of all three mirrors would lead to  $\delta S_h/S_h = \delta_r$  twice as large as expression (4.48). Inserting the advanced LIGO finesse  $\mathcal{F} \simeq 50$  and mean-square beam radius  $\langle r^2 \rangle = (6.95\text{cm})^2$  (fiducial mesa) and  $(4.70\text{cm})^2$  (fiducial Gaussian), and constraining the increase in  $S_h$  to no more than one per cent, we would then obtain

$$\theta_{1\%}^{\text{MH}} \simeq 0.4 \times 10^{-8}, \quad \theta_{1\%}^{\text{sph}} \simeq 0.6 \times 10^{-8},$$

As we have seen, an output mode cleaner will remove this increase of  $S_h$ , making these constraints no longer needed.

### J. Decrease in Signal Strength Due to Mirror Figure Errors

The loss of signal strength and resulting increase in  $S_h$ , caused by mirror figure errors, is given by the same equation  $S_h \propto 1 + 2\delta_0 + 2\delta_s + \delta_t + \{\delta_r \text{ or } 0\}$  as for mirror tilt [Eq. (4.31)], but now  $\delta_\ell$  is the fraction of power in the parasitic components of mode  $u'_\ell$  due to figure errors rather than tilt.

#### 1. Carrier light in arm cavity

Deformations of the ITM and ETM, with optimized tilt compensation, drive a fraction  $\delta_0 = \beta_{1cE}^2 + \beta_{1cI}^2$  into parasitic modes [Eqs. (4.22) and (4.23)]. Assuming the same peak-to-valley deformations  $\Delta z$  in the two mirrors' central regions, we obtain for the fractional increase in gravitational-wave noise

$$\left( \frac{\delta S_h}{S_h} \right)^{\text{MH}} = 2\delta_0 = 4\beta_{1c}^2 \simeq 0.01 \left( \frac{\Delta z}{15\text{nm}} \right)^2. \quad (4.50)$$

Correspondingly, to keep the noise increase below one per cent, we must constrain the ITM and ETM deformations to

$$\Delta z_{1\%}^{\text{MH}} \simeq 15\text{nm} \quad (4.51)$$

We have not carried out an analysis of the influence of the ITM and SRM mirror deformations on the fiducial Gaussian arm cavity modes, and so cannot say what the analogous constraint is in the Gaussian case.

<sup>12</sup> In [14] this equation was missing the factor 2, which produced factor 2 errors in the resulting constraints on tilt; cf. Sec. IV,E,5 of [14].

<sup>13</sup> LIGO-I has asymmetric arm cavities; the 2.9 cm that we use is the root mean square of the beam radii on the ITM and ETM.

<sup>14</sup> Their result (end of Sec. 2.A) is  $\theta < 1.0 \times 10^{-8}$  for the tilts in pitch and in yaw, corresponding to a constraint  $\theta < \sqrt{2} \times 10^{-8} \simeq 1.4 \times 10^{-8}$  on the magnitude of the vectorial tilt, for an 0.005 fractional decrease in amplitude signal to noise, which corresponds to our one per cent increase in  $S_h$ .

## 2. Signal light in arm cavity

As for tilt, so also for figure errors, the SR cavity amplifies the influence of the errors  $\Delta z$  by a factor  $\mathcal{A}$  [Eq. (4.35)], so the ITM and SRM deformations move a fraction  $\delta_s = \mathcal{A}^2(\beta_{1cI}^2 + \beta_{1cSR}^2)$  of the arm cavity's signal light into parasitic modes. When the two figure errors have the same magnitude and we wish to keep the resulting loss of signal power and increase of  $S_h$  below one per cent, this gives rise to constraints on the ITM and SRM figure errors that are  $1/\mathcal{A}$  more severe than (4.51). Using the values (4.36) of  $\mathcal{A}$  for our three interferometers (wide-band, narrowbanded at 500 Hz and narrowbanded at 1000 Hz), and increasing the limit for the 1000-Hz narrowbanded case by a factor 2 due to failure of the geometric-optics limit [cf. Eq. (4.39) and associated discussion], we obtain the constraints

$$\begin{aligned} \Delta z_{1\%}^{\text{MH WB}} &\simeq 55\text{nm}, \\ \Delta z_{1\%}^{\text{MH 500}} &\gtrsim 10\text{nm}, \text{ with a guess of } \simeq 10\text{nm}, \\ \Delta z_{1\%}^{\text{MH 1000}} &\gtrsim 2.6\text{nm}, \text{ with a guess of } \simeq 5\text{nm}. \end{aligned} \quad (4.52)$$

## 3. Transmission of signal light through SR cavity

By the same analysis as for mirror tilt (Sec. IV I4), deformations  $\delta z(x, y)$  of the ITM and SRM by the same peak-to-valley amounts  $\Delta z$  produce an increase in  $S_h$  given by

$$\begin{aligned} \left( \frac{\delta S_h}{S_h} \right)_{\text{transmission}} &= \delta_t = 2\mathcal{B}^2 k^2 \langle (\delta z)^2 \rangle \\ &= \frac{1}{4} \mathcal{B}^2 k^2 (\Delta z)^2 \end{aligned} \quad (4.53)$$

[cf. Eq. (4.44) with  $\langle (\delta z)^2 \rangle = \langle (\theta r \sin \varphi)^2 \rangle = \frac{1}{2} \langle r^2 \rangle \theta^2$ ]. Here  $\langle (\delta z)^2 \rangle$  is the mean square deviation of ITM or SRM height from the desired figure, and we have approximated this by half the squared amplitude of mirror height fluctuations, which is  $1/8$  the square of the peak to valley height fluctuations,  $(\Delta z)^2/8$ . Inserting the values of  $\mathcal{B}$  for our three interferometers [Eq. (4.43)] and requiring that  $S_h$  increase by no more than one per cent, we obtain the following constraints on the ITM and SRM peak to valley deformations:

$$\begin{aligned} \Delta z_{1\%}^{\text{MH WB}} &= \Delta z_{1\%}^{\text{sp}}^{\text{WB}} \simeq 2\text{nm}, \\ \Delta z_{1\%}^{\text{MH 500}} &= \Delta z_{1\%}^{\text{sp}}^{\text{500}} \lesssim 1\text{nm}, \text{ with a guess } \simeq 1\text{nm}, \\ \Delta z_{1\%}^{\text{MH 1000}} &= \Delta z_{1\%}^{\text{sp}}^{\text{1000}} \lesssim 0.5\text{nm}, \text{ with a guess } \simeq 1\text{nm}. \end{aligned} \quad (4.54)$$

Here as in Eqs. (4.52), (4.46) and (4.39), the breakdown of the geometric optics limit in the SR cavity has dictated a lower limit and a guess for the narrowbanded interferometers.

These are the most serious of our constraints on the mirror figures of advanced interferometers, and they are the same for fiducial mesa and fiducial Gaussian beams, because transmission through the SR cavity is governed (at least roughly) by geometric optics. The one small difference is that the central region over which the peak-to-valley deformations are constrained (the region containing  $\sim 95$  per cent of the light power) is larger for the fiducial MH mirrors (central radius about 10 cm) than for the fiducial Gaussian mirrors (central radius about 8 cm).

The mirror-figure constraint (4.54) is sufficiently severe, at least in the case of narrowbanded interferometers, that it might be worth considering reducing the degeneracy of the SR cavity by making the entrance faces of the ITM's into lenses that bring the signal light (and inevitably also the carrier light) to a focus somewhere near the SRM (and PRM). Since the constraint (4.54) is the same, whether the mirrors are MH or spherical, this recommendation is not dependent on whether mesa beams are implemented.

## 4. Reference light for baseline readout

As for mirror tilt, so for figure errors, the output mode cleaner in advanced LIGO makes  $S_h$  insensitive to the loss of reference light into parasitic modes.

## 5. Transmission of RF reference light through power recycling cavity without an output mode cleaner

In the LIGO-I case of no output mode cleaner and heterodyne readout with RF sideband light, the loss of reference light to parasites does increase  $S_h$ . By the same argument as for mirror tilt (Sec. IV I6), the net increase of  $S_h$  due to deformations  $\delta z(x, y)$  of the ITM and PRM is<sup>15</sup>

$$\begin{aligned} \left( \frac{\delta S_h}{S_h} \right)_{\text{reference}} &= \delta_r = 2 \left( \frac{2\mathcal{F}}{\pi} k \right)^2 \langle (\delta z)^2 \rangle \\ &= \frac{1}{4} \left( \frac{2\mathcal{F}}{\pi} k \right)^2 (\Delta z)^2 \end{aligned} \quad (4.55)$$

[cf. Eq. (4.48) with  $\langle (\delta z)^2 \rangle = \langle (\theta r \sin \varphi)^2 \rangle = \frac{1}{2} \langle r^2 \rangle \theta^2$ ]. For advanced LIGO with RF readout and no mode cleaner, there is an extra factor 2 in Eq. (4.55) due to change of configuration of the RF cavity (the added SRM and the light encountering the ITM twice on each round trip). Inserting the finesse of LIGO-I ( $\mathcal{F} \simeq 105$ ) and advanced LIGO ( $\mathcal{F} \simeq 50$ ) and insisting that  $S_h$  not be

<sup>15</sup> In [14] the factor 2 in  $(2\mathcal{F}k/\pi)^2$  was missing, which produced factor 2 errors in the resulting constraints (4.56) on  $\Delta z$ ; cf. Sec. IV F 4 of [14].

increased by more than one per cent, we obtain the following constraints on the central-region peak-to-valley deformations of the PRM and SRM:

$$\begin{aligned}\Delta z_{1\%}^{\text{LIGO-I}} &= 0.5\text{nm} , \\ \Delta z_{1\%}^{\text{MH}} &= \Delta z_{1\%}^{\text{sph}} = 0.5\text{nm} .\end{aligned}\quad (4.56)$$

These constraints are rather severe, but for advanced LIGO the constraint is actually irrelevant because of the output mode cleaner (and the planned use of homodyne readout rather than heterodyne).

## V. CONCLUSIONS AND FUTURE RESEARCH

The thermoelastic benefits of MH mirrors are sufficiently great, and the tightened constraints that they place on mirror figures, positions and tilts are sufficiently modest, that MH mirrors have been adopted by the LSC as an option for advanced LIGO, and will be incorporated into future modeling along with spherical mirrors.

Two methods of manufacturing MH mirrors are being explored by the LIGO Laboratory: diamond cutting, and evaporative coating. The immediate goal is to determine the accuracy and reproducibility with which the desired MH mirror figures can be produced by each of these methods.

If MH mirrors are to be considered seriously for advanced LIGO, it is necessary to develop laboratory experience with them and with the mesa-beam optical cavities that they produce. An experimental effort in this direction has been initiated by Phil Willems of the LIGO Laboratory at Caltech.

As we have discussed in Secs. IV H and IV J 3, the constraints on mirror figure in the recycling cavities are rather worrisome for both spherical mirrors and MH mirrors. More accurate studies of this are needed. As one aspect of these studies, it is important to check our geometric-optics-based claims that the fiducial MH recycling cavities are not much more sensitive to mirror figure errors than the fiducial Gaussian-beam cavities.

If the recycling-cavity-induced constraints on mirror figure are found to be as serious as our estimates suggest, then it seems worthwhile to carry out studies of the option of converting the input faces of the ITM's into lenses that make the recycling cavities much less degenerate. PhD students in Thorne's research group may carry out these studies as part of the broadening experience that is a standard part of their education.

Bill Kells has suggested the possibility of operating the advanced LIGO interferometers initially with spherical mirrors and Gaussian beams, and later switching to mesa beams by altering only the ETM's. It seems to us that this option is worth detailed study. If the ITM input faces are turned into lenses that reduce the near degeneracy of the recycling cavities, then it might be possible to keep the lenses weak enough that the figures of the recycling mirrors can be the same for Gaussian and mesa beams,

while still relaxing the mirror figure constraints to an acceptable level. This needs study.

## Acknowledgments

For helpful discussions and advice we thank, among others, Raymond Beausoleil, Alessandra Buonanno, Vladimir Braginsky, Yanbei Chen, Peter Fritschel, Greg Harry, Bill Kells, David Shoemaker, Robert Spero, Ken Strain, Rai Weiss, Phil Willems, Stan Whitcomb, Farid Khalili, Mike Zucker, and especially Garilynn Billingsley and Guido Müller. We thank Billingsley for providing us with the mirror figure map (Fig. 6) used in our study of the influence of mirror figure errors, we thank Müller for a detailed critique of the manuscript (in his role as LSC referee) which resulted in significant changes, and we thank Patrice Hello, Jean-Yves Vinet, Brett Bchner, and others who developed and refined the FFT code that ED'A adapted for use in her calculations of the influence of mirror tilt, displacement, and figure errors. This research was supported in part by NSF grants PHY-0098715 and PHY-0099568, by the Russian Foundation for Fundamental Research grants #96-02-16319a and #97-02-0421g, and (for SPV) by the NSF through Caltech's Institute for Quantum Information.

## APPENDIX: APPROXIMATE FORMULAE FOR MESA MODES

By inserting into Eq. (2.5) the asymptotic expansion (at large argument) for the Bessel function

$$I_0(z) = \frac{1}{\sqrt{2\pi z}} e^z , \quad (1)$$

setting  $b = 1$ ,  $r_o = D - \xi$ , and

$$\alpha = \sqrt{(1+i)/2} , \quad (2)$$

we bring Eq. (2.5) into the approximate form

$$U(D, r) = \sqrt{\frac{\pi}{\alpha^2 r}} \int_0^D \sqrt{D - \xi} \exp[-\alpha^2(r - D + \xi)^2] d\xi . \quad (3)$$

By expanding  $\sqrt{D - \xi}$  as a power series in  $\xi/D$  up to some order  $n$ , and then performing the integral in Eq. (3) analytically, we obtain expressions for  $U(D, r)$  with various accuracies. The least accurate expression,  $n = 0$  (obtained by setting  $\sqrt{D - \xi} = \sqrt{D}$ , integrating, and discarding a term proportional to  $\text{erfc}(\alpha r)$  that is negligible compared to  $\text{erfc}[\alpha(r - D)]$  at the relevant radii,  $r \sim D$  or larger) is

$$U_0(D, R) = \frac{\pi}{2\alpha^2} \sqrt{\frac{D}{r}} \text{erfc}[\alpha(r - D)] . \quad (4)$$

Here  $\text{erfc}(z)$  is the complementary error function,  $1 - \text{erf}(z)$ . At order  $n = 3$  we get a much more accurate



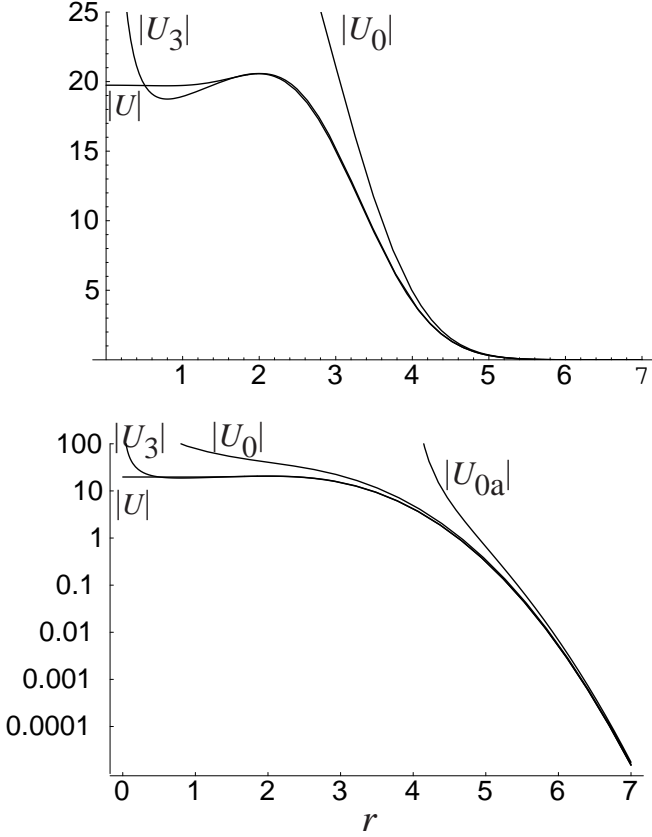


FIG. 10: Comparison of the moduli of the exact flat-topped mode  $U(4, r)$ , the zero-order approximation  $U_0(4, r)$  [Eq. (4)], the third-order approximation  $U_3(4, r)$  [Eq. (5)], and the asymptotic approximation to the zero-order approximation,  $U_{0a}(4, r)$  [Eq. (7)]. Top: linear plot; bottom: logarithmic plot.

expression:

$$\begin{aligned}
 U_3(D, r) = & \frac{1}{64\alpha^5 D^2 \sqrt{Dr}} \\
 & \times \left\{ \pi \left[ \alpha^3 (2r^3 - 10Dr^2 + 30D^2r + 10D^3) + \alpha(3r - 5D) \right] \right. \\
 & \times \left[ \operatorname{erfc}[\alpha(r - D)] - \operatorname{erfc}[\alpha r] \right] \\
 & + 2\sqrt{\pi} \left[ e^{-\alpha^2 r^2} [\alpha^2 (15D^2 - 5Dr + r^2) + 1] \right. \\
 & \left. \left. - e^{-\alpha^2 (r-D)^2} [\alpha^2 (11D^2 - 4Dr + r^2) + 1] \right] \right\}. \quad (5)
 \end{aligned}$$

Here  $\operatorname{erfc}$  is the complementary error function,  $\operatorname{erfc}(z) = 1 - \operatorname{erf}(z)$ .

The two approximations  $U_0(4, r)$  and  $U_3(4, r)$  are compared with the exact mode  $U(4, r)$  in Fig. 10. At  $r > 2$ ,  $U_3$  is highly accurate; at  $r > 5$ ,  $U_0$  is highly accurate. The analytic formula (4) for  $U_0$  shows that the diffraction-induced tail of this mode falls off very rapidly outside  $r = D$  — slightly more rapidly than would the tail of a Gaussian centered on  $r = D$ . Of course, this is to be expected since  $U(D, r)$  is constructed from a superposition of Gaussians that are centered on radii  $\leq D$ .

A useful but cruder approximation to  $U(D, r)$  can be obtained by inserting the asymptotic expansion of  $\operatorname{erfc}[\alpha(r - D)]$  into Eq. (4) for  $U_0$ . The result is

$$U_{0a}(D, r) = \frac{\sqrt{\pi D/r}}{2\alpha^3(r - D)} e^{-\alpha^2(r-D)^2}, \quad (6)$$

which has a modulus

$$|U_{0a}(D, r)| = \sqrt{\frac{\pi D}{2r}} \frac{e^{-(r-D)^2/2}}{r - D}. \quad (7)$$

This modulus is accurate to within several tens of percent in the regime of interest for diffraction,  $D \sim 4$  and  $R \gtrsim 6$  (in units of  $b$ ). By inserting this approximation into Eqs. (2.11) and (2.7) for diffraction losses in the clipping approximation, we deduce that the diffraction losses for mesa beams scale with beam-spot radius  $D$  as

$$\mathcal{L}_{\text{clip}}^{\text{mesa}} \propto \exp(-2RD/b^2). \quad (8)$$

Here  $R$  is the mirror radius and we have restored the diffraction lengthscale  $b$ , which was set to one throughout this appendix.

- 
- [1] The LIGO-I Collaboration, Nucl. Instrum. Meth. **A517**, 154 (2004).
  - [2] The LIGO-I Collaboration, Phys. Rev. D **69**, 082004, 102001, 122001, and 122004 (2004).
  - [3] C. Cutler and K. Thorne, in *General Relativity and Gravitation: Proceedings of the 16th International Conference*, edited by N. Bishop and S. Maharaj (World Sci-

- entific, 2002), p. 72.
- [4] D. Shoemaker and the LIGO Scientific Collaboration, LIGO Report Number M030023-00 (2003), URL <http://admbdsvr.ligo.caltech.edu/dcc/>.
- [5] V. Braginsky, M. Gorodetsky, and S. Vyatchanin, Phys. Lett. A **264**, 1 (1999).
- [6] Y.-T. Liu and K. S. Thorne, Phys. Rev. D **62**, 122002

- (2000).
- [7] A. Buonanno and Y. Chen, Phys. Rev. D **64**, 042006 (2001).
  - [8] A. Buonanno and Y. Chen, Phys. Rev. D **65**, 042001 (2002).
  - [9] A. Buonanno and Y. Chen, Phys. Rev. D **67**, 062002 (2002).
  - [10] E. d'Ambrosio, R. O'Shaughnessy, and K. Thorne, LIGO Report Number G000223-00-D (16 August 2000), URL <http://admbdbsrv.ligo.caltech.edu/dcc/>.
  - [11] V. Braginsky, E. d'Ambrosio, R. O'Shaughnessy, S. Strigin, K. Thorne, and S. Vyatchanin, LIGO Report Number G010151-00-R (16 March 2001), URL <http://admbdbsrv.ligo.caltech.edu/dcc/>.
  - [12] V. Braginsky, E. d'Ambrosio, R. O'Shaughnessy, S. Strigin, K. Thorne, and S. Vyatchanin, LIGO Report Numbers G010333-00-D and G010297-00-D (15 August 2001), URL <http://admbdbsrv.ligo.caltech.edu/dcc/>.
  - [13] V. Braginsky, E. d'Ambrosio, R. O'Shaughnessy, S. Strigin, K. Thorne, and S. Vyatchanin, LIGO Report Number G020543-00-R (6 September 2002), URL <http://admbdbsrv.ligo.caltech.edu/dcc/>.
  - [14] V. Braginsky, E. d'Ambrosio, R. O'Shaughnessy, S. Strigin, K. Thorne, and S. Vyatchanin, LIGO Report Number T030009-00-R (23 January 2003), URL <http://admbdbsrv.ligo.caltech.edu/dcc/>.
  - [15] R. O'Shaughnessy, S. Strigin, and S. Vyatchanin, Phys. Rev. D (2003), submitted.
  - [16] E. D'Ambrosio, Phys. Rev. D **67**, 102004 (2003).
  - [17] P. Fritschel, N. Mavalvala, D. Shoemaker, D. Sigg, M. Zucker, and G. Gonzalez, Applied Optics **37**, 6734 (1998).
  - [18] G. Müller, LIGO Report Number G010078-00-D (2001).
  - [19] A. Siegmann, *An Introduction to Lasers and Masers* (McGraw-Hill, 1971).
  - [20] Y. Levin, Phys. Rev. D **57**, 659 (1998).
  - [21] L. Finn and the LIGO Scientific Collaboration, *Bench*, URL <http://fiji.nirvana.phys.psu.edu/~lsf/Benchmarks/>.
  - [22] B. Bochner, Ph.D. thesis, MIT (1998), LIGO Report Number P980004-00-R, URL <http://admbdbsrv.ligo.caltech.edu/dcc/>.